REVISION 1

Atomic structure and formation mechanism of (101) rutile twins from Diamantina (Brazil)

Nina Daneu[1], Aleksander Rečnik[1] and Werner Mader[2]

[1] Department for Nanostructured Materials, Jožef Stefan Institute, Jamova 39, 1000 Ljubljana, Slovenia

[2] Institut für Anorganische Chemie, Universität Bonn, Römerstrasse 164, 53117 Bonn, Germany

Abstract

We studied the atomic structure and the chemical composition of (101)-type rutile (TiO_2) twins from Diamantina in Brazil by electron microscopy methods to resolve the mechanism of their formation. The twin boundaries were studied in two perpendicular orientations to reveal their 3D structure. The presence of a precursor phase, such as Al-rich hydroxylian pseudorutile (HPR; kleberite), during the initial stages of the crystallization appears to be the necessary condition for the formation of (101) twins of rutile at this locality. The precursor with a tivanite-type structure serves as a substrate for the topotaxial crystallization of rutile. Depending on the the initial crystallization pattern the rutile can grow either as a single crystal or as a twin. During the progressive crystallization of the rutile Al-rich oxyhydroxide (diaspore, α-AlOOH) clusters are concentrated at the centre of the precursor where they are pinned to the twin boundary as the precursor is fully recrystallized into rutile. At the increased temperatures the remaining diaspore precipitates are converted to corundum (α-Al_2O_3), while the two crystal domains continue to grow in the (101) twin orientation. In addition to the primary (101) twin, series of secondary {101} twins are formed in order to accommodate the residual tensile stress caused by the diaspore-to-corundum transformation. Based on the observed corundum – rutile $[0001]_C(11\bar{2}0)_C \parallel [010]_R(101)_R$ and ilmenite – rutile $[0001]_I(1\bar{1}00)_I \parallel [010]_R(301)_R$ crystallographic relations a unified mechanism of the genesis of the {101} and {301} reticulated sagenite twin clusters is proposed.

Keywords: rutile, alumina, dehydration, exsolution, mobility, epitaxy, twinning

Introduction

Diamantina, Brazil is world's famous for its sharp, deep-red translucent crystals of rutile (TiO_2). The majority of the rutiles here are repeatedly twinned on {301} and {101} planes, forming complex 2D sagenite networks. In our earlier study on the origin of (301) twins from this locality (Daneu *et al.* 2007) we identified a few-nanometers-thick interfacial lamella of Al-rich ilmenite ($FeTiO_3$), coherently intergrown with the twin interface. The fine nanostructural features within this lamella indicated that the (301) twins nucleated on the tivanite-type Ti-Fe-Al oxyhydroxide, which subsequently dehydrated to form ilmenite during the crystallization of rutile. This study demonstrated that the formation of (301) twins of rutile is not accidental but a consequence of topotaxial growth on a structurally related oxyhydroxide precursor.

On the other hand, very little is known about the formation of the other type of twins in rutile, *i.e.*, (101) twins, which are generally even more abundant than the (301) twins. In numerous studies of natural and synthetic rutiles, different mechanisms of twinning have been proposed. The formation of twins in natural rutiles is most often related to the intergrowths/overgrowths of rutile with structurally related minerals that crystallize in the corundum-type structures (*e.g.*: hematite, ilmenite, corundum). All these minerals possess a similar hexagonal close-packed (*hcp*) oxygen sublattice, which enables simple transitions among them by exsolution, epitaxy or intergrowth (Armbruster 1981, Boudeulle 1994; Force *et al.* 1996). In synthetic rutile, twinning has been explained either as a result of stress (Takeuchi & Hashimoto 1990, Suzuki *et al.* 1991), as an efficient mechanism of local energy reduction in nonstoichiometric TiO_{2-x} (Reece & Morell 1991), or by accidental attachment of TiO_2 nanocrystals to form different types of interfaces, including twin boundaries, during the initial stages of crystal growth (Penn & Banfield 1998). {301} and {101} twins are also observed in nanocrystalline rutile produced via miscellaneous synthesis pathways (Li *et al*. 1999, Lu *et al*. 2012), whereas their formation mechanisms remain unclear. The epitaxially induced twinning of rutile has been reported during the chemical leaching of ilmenite (Putnis 2009; Janssen *et al.* 2010).

For the present study we selected (101) twins of rutile from the same locality as the previously studied (301) twins (Daneu *et al*. 2007). As both types of twins occur together we may anticipate the same growth

conditions and the only difference apart from the crystallography would be variations in the local chemistry during the crystal growth. Based on a structural analysis of the (101) twins we propose a mechanism for their formation.

Experimental Methods

Specimen preparation. For investigations of the twin interface a well-developed (101) rutile twin from Diamantina, shown in Figure 1a, was used. As with most of the specimens from this locality, the crystal showed no attachment point, and it may well be assumed that the rutile crystals grew as floaters. The (101) twin boundary symmetrically splits the crystal into two halves, coinciding at an angle of 114.4°, which directly corresponds to the angle enclosed by the crystallographic *c*-axes between the two rutile domains. In addition to the main (101) twin boundary, the crystal contains numerous planar defects following different sets of {101} planes. These are visible as thin streaks on the right-half of the twin and in the close-up image near the main twin boundary. One set of streaks is parallel to the (101) planes, while the other is parallel to the ($\bar{1}$01) planes. To improve the chances of finding the nucleation point of the twinned crystal, where the elements that triggered its formation are likely to be present, the samples were cut from the central section of the twin (Daneu *et al.* 2007), as illustrated in Figure 1b. Thin slices with the main (101) twin boundary placed at the centre were cut into two perpendicular low-index orientations [010] and [10$\bar{1}$)], in which the boundary can be studied edge-on from the front and top view, respectively. A petrographic microscope (Axio Imager Z1m, Zeiss GmbH, Germany) was used to determine which of the parallel defects is the main (101) twin boundary. In addition to the main twin, the slices also contained an abundance of {101} planar faults that are present in the vicinity of the interface. The slices were mounted into alumina rings and fixed with an epoxy resin for TEM specimen preparation. Discs with thin slices of rutile were mechanically thinned to *ca*. 100 µm and polished. The specimens were dimpled from one side to a final thickness of about 25 µm in the dimple centre. Finally, the samples were ion-milled (BAL-TEC RES 010, Balzers, Liechtenstein) using 4 kV/1.2 mV Ar^+ ions from both sides at incidence angles of 10° until perforation to obtain electron-transparent sections.

Analytical methods. Larger sections of the main (101) twin interface were first inspected in a high-resolution scanning electron microscope with a field-emission electron source (FEG-SEM; JSM-7600F, Jeol Ltd., Tokyo, Japan) and analyzed using energy-dispersive spectroscopy (EDS; SDD-Si, Jeol Ltd., Tokyo, Japan). The local structure and chemistry of the twin boundary were analyzed by transmission electron microscopy (TEM). For the TEM analyses we used a conventional 200-kV TEM with a LaB_6 source (JEM-2100, Jeol Ltd., Tokyo, Japan) and a 200-kV TEM with a field-emission electron source (FEG-TEM; JEM-2010F, Jeol Ltd., Tokyo, Japan) equipped with a Si(Li) energy-dispersive spectrometer (EDS; Model Link ISIS-300, Oxford Instruments, Oxfordshire, U.K.).

Results

In optically anisotropic materials, such as rutile, twins are readily identified using a petrographic microscope revealing characteristic extinctions at specific angles under crossed Nicols. Under the condition, when one twin domain is brought to extinction (dark), the other domain appears bright. Using this intense contrast difference between the two domains, the main twin boundary is easily identified. In addition to this general contrast change, thin dark stripes of parallel secondary defects become visible in the adjacent (bright) domain, implying that they occur in narrow {101} pairs, while according to their reverse extinction with the main twin domains it can be concluded that these defects are {101} twins, too. No such parallel defects were observed in (301) twins from the same locality (Daneu *et al*. 2007).

Primary and secondary {101} twin boundaries in rutile

The samples were further investigated by scanning electron microscopy. To search for the presence of secondary phases along the twin interface, *e.g.* an interfacial lamella of ilmenite in a (301) twin, backscattered electron (BSE) imaging was implemented. Figure 2 shows a SEM/BSE image of a TEM sample prepared and oriented close to the [010] zone axis. Here we exploit channeling effects to obtain a decent con-

trast between the twin domains. Namely, except for composition (Z-contrast), BSEs are also sensitive to the specimen's topography and crystallographic orientation. If a crystal is oriented close to a low-index zone axis many electrons are lost by channeling down the atomic columns, resulting in a lower BSE yield (dark contrast); however, if the crystal is tilted only slightly out of the zone axis more electrons are backscattered, which immediately produces a bright BSE contrast. Due to this effect, domain I appears darker than domain II, enabling easy identification of the twin interfaces in Figure 2. Smooth polishing provided by ion-milling allows us to distinguish fine nanostructural features, otherwise invisible in samples with rough surfaces. If we take a closer look at the main twin boundary, we observe that it is decorated with numerous, up to 200 nm large, black inclusions. A darker contrast implies the presence of a secondary phase containing elements with significantly lower average atomic number *Z*, than the surrounding rutile. According to the EDS analysis the inclusions are Al-rich. While the majority of the inclusions are located at the main (101) twin boundary, only few were observed on secondary twins, and even fewer in the bulk rutile. The presence of inclusions suggests that they might be remnants from the nucleation stage of the primary twin. Furthermore, the inclusions at the primary twin boundary were present only in the samples cut from the central part of the crystal (*see* Figure 1b), while they were absent in crystal segments that were distant from the centre.

Analysis of (101) twin boundaries in [010] projection

In the TEM we observed that in segments prepared from the central part of the twinned crystal secondary {101} twins are quite abundant and at first glance they complicate identification of which of the parallel defects is actually the primary (101) twin boundary. The fact that they are void of precipitates and that they occur in pairs is of some assistance. Figure 3 shows a TEM image of a thin crystal section containing several parallel {101} twin boundaries. The width of the twinned domains ranges from 20 nm up to several hundred nanometers. They are separated by thicker blocks of rutile in the primary orientation. The twinned orientation of the crystal domains is confirmed by selected area electron diffraction (SAED) patterns, shown

in Figures 3b-3d, suggesting a 180° rotation around the (101) plane normal. The twinned domains can best be visualized by dark-field (DF) imaging using any of the unique reflections that are sufficiently intense. DF-TEM image shown in Figure 3a is produced by $(10\bar{1})$ reflection (marked in Figure 3c) of domain I that is not shared by domain II. As a result, the twinned domains appear dark. The opposite contrast can be produced by $(10\bar{1})$ reflection of domain II. At higher magnifications, as shown in the HRTEM image in Figure 3e, {101} twin boundaries are atomically sharp, without the presence of any secondary phase along the contact plane. The spacings of the (101) planes across the twin interface are regular, showing no measurable dilatation or contraction of the crystal lattice. The spatial difference EDS analysis on twin boundaries using a small beam diameter (of *approx.* 5 nm) showed that the composition of the twin boundaries is identical to that of bulk rutile. The atomic structure of simple (101) twin boundaries in rutile is consistent with the one proposed by Takeuchi and Hashimoto (1990). According to this model the twin boundary is located at the $Ti_{(101)}$-plane. The twin operation that describes the observed crystal lattice translation is a 180° rotation about the [101]-axis, or a mirror operation at the $Ti_{(101)}$-plane, followed by a $\frac{1}{2}\cdot\langle 111\rangle$ shift of the twinned domain. This translation produces a mirror symmetry for the cation sublattice, whereby all Ti atoms remain octahedrally coordinated by O atoms.

In contrast to the secondary twin boundaries, the primary twin boundary is characterized by numerous precipitates lined along the interface. The TEM-EDS analysis confirmed that the precipitates contain Al as the main constituting cation; however, at least some Ti signal was present in all the EDS spectra, even in analyses with a nanometer-sized beam in FEG-TEM. The Ti signal is likely to be caused by X-ray fluorescence, coming from stray X-rays hitting the entire rutile sample, which is difficult to avoid. Figure 4a shows a low-magnification TEM image of the primary (101) twin boundary in rutile oriented in the $[010]_R$ projection. In this projection the precipitates show a characteristic lenticular shape, elongated along the twin interface. A diffraction pattern of the region including the Al-rich precipitate is shown in Figure 4b. The SAED pattern contains diffraction spots from both rutile domains in the (101) twin orientation and additional reflections from the precipitate, marked by arrows. The *d*-spacings of these reflections best correspond to α-Al_2O_3 (corundum) in the $[0001]_C$ projection. The arrangement of the reflections from corundum and rutile

obeys the following epitaxial orientation relationship: $[0001]_C(11\bar{2}0)_C \parallel [010]_R(101)_R$. The structural matching in reciprocal space is illustrated in Figure 4c. Already at first glance, the matching of the two lattices appears to be very good. The misfit (δ) between the two lattices can be calculated according to the following equation (Löffler & Mader 2003):

$$\delta = 2 \cdot \left| \frac{d_C - d_R}{d_C + d_R} \right| \quad (1)$$

where d_C and d_R represent the projected Al-Al distances in the corundum and the Ti-Ti distances in the rutile normal to the $(11\bar{2}0)_C$ and $(101)_R$ interface planes and parallel with the vectors $[0001]_C$ and $[010]_R$, respectively. In corundum (a = 0.47570 nm, c = 1.29877 nm; Kirfel & Eichhorn 1990), the Al-Al distance is $d_C = a/\sqrt{3}$ and amounts to 0.2746 nm and in rutile (a = 0.45937 nm, c = 0.29587 nm; Abrahams and Bernstein 1971), the projected distance between the Ti atoms is $d_R = \frac{1}{2}\sqrt{a^2 + c^2}$, which is 0.2732 nm.

The calculated misfit (Eq. 1) between corundum and rutile is expectedly small and amounts to 0.51%. Correspondingly, we could expect one misfit dislocation on every ~200 lattice planes; however, the HRTEM study of the interface in this projection showed no misfit dislocations. According to Gao *et al*. (1992) such a small misfit may be easily compensated at the interface steps. Figure 4d shows a perfectly coherent section of the corundum–rutile interface with smooth transitions of the lattice planes from the corundum into the rutile lattice. In this schematic structural model, the width of the corundum layer is 1.7 nm, whereas in reality the width of the corundum precipitates reaches several tens of nanometers.

Analysis of (101) twin boundaries in the $[10\bar{1}]_R$ projection

In order to obtain complete 3D information about the (101) twin boundary and the corundum–rutile interface, their structures were further analyzed in the perpendicular projection, $[10\bar{1}]_R$ (*see* Figure 1b). A low-magnification TEM image of the primary (101) twin boundary with three equally spaced corundum precipitates, and the fourth one etched away by ion-milling in the thin crystal part, is shown in Figure 5a. In this orientation, the precipitates exhibit a quite regular rectangular shape. The uniform length of the pre-

cipitates in the $[10\bar{1}]_R$ projection, not much different to that in the $[010]_R$ projection, suggests that they have a square-like tabular morphology, flattened by the $(11\bar{2}0)_C$ planes. The SAED pattern in Figure 5b, recorded from the area including one of the precipitates shows additional reflections corresponding to corundum in the $[1\bar{1}00]_C$ projection. A calculated diffraction pattern is shown in Figure 5c. The rutile-corundum orientation relationship is $[1\bar{1}00]_C(11\bar{2}0)_C \parallel [10\bar{1}]_R(101)_R$, which is a 90° equivalent of $[0001]_C(11\bar{2}0)_C \parallel [010]_R(101)_R$, confirming the unique placement of the corundum precipitates along the primary (101) twin interface. Next to the precipitates, the (101) contact between the two rutile domains is simple, without any measurable dilatation or contraction and no shift of the $(010)_R$ lattice planes parallel to the twin boundary, confirming a simple mirror-symmetric translation of the cation sublattice, as suggested by Suzuki et al. (1991).

If the misfit between the rutile and corundum lattice planes across the twin boundary is calculated (Eq. 1) for this orientation using $d_C = (0003)_C = 0.4329$ nm for corundum and the corresponding $d_R = (010)_R = 0.4594$ nm for rutile, a value of 5.92% is obtained. Such a large misfit can only be compensated by misfit dislocations. To calculate the actual distance (D) between the misfit dislocations (Vernier period of a misfit), when one additional plane of the smaller lattice is compensated, the following equation can be used:

$$D = \frac{d_C \cdot d_R}{|d_C - d_R|} \quad (2)$$

yielding a theoretical value of ~7.53 nm (Gao *et al*. 1992). The closest integers matching this value are 17-18 planes of corundum that would roughly correspond to 16-17 equivalent planes of rutile, after which a dislocation would be expected to form (*see* Fig. 5d).

As observed from the experimental HRTEM image of the corundum-rutile contact in Figure 5d, the actual distance between the misfit dislocations in rutile is larger and amounts to ~11.5 ± 1.1 nm. To explain this significantly larger spacing, the *actual* misfit between the lattice planes $(010)_R$ and the $(0003)_C$ has to be determined. To obtain reliable experimental values this is done best by measuring the lengths of diffraction vectors $\vec{g}_R = (040)_R = 8.59$ nm^{-1} and $\vec{g}_C = (000\,12)_C = 8.94$ nm^{-1}, from the original diffraction pattern shown in

Figure 5b. The misfit (δ') between the lattice planes in real space is then obtained by introducing the measured $d_R' = |\vec{g}_R|^{-1}$ and $d_C' = |\vec{g}_C|^{-1}$ in Equation 1, which results in a value of 3.9%. Taking into account that $\vec{g}_R$ in bulk rutile does not differ from that measured near the precipitates we may assume that most of the lattice deformations are accumulated in corundum, while the rutile lattice is largely undistorted. Assuming a regular rutile lattice, the actual $(0003)'_C$ lattice plane spacing of the corundum precipitate can be calculated by:

$$d_C' = \frac{1 - \frac{1}{2}\cdot\delta'}{1 + \frac{1}{2}\cdot\delta'} \cdot d_R \qquad (3)$$

which gives $d'_C \approx 0.4418$ nm. Our d'_C value appears to be significantly larger than the corresponding spacing of the $d_C = (0003)_C$ planes of corundum ($d_C = 0.4329$ nm; Kirfel & Eichhorn 1990). Using Equation 2, the Vernier period of the misfit, *i.e.* the dislocation spacing between rutile and the precipitate corundum, can be calculated to $D \approx 11.5$ nm. This value matches the observed spacing between the misfit dislocations in the experimental HRTEM image in Figure 5d. These results indicate that the corundum in the precipitates is considerably expanded along the *c*-axis. The porosity of the corundum precipitates result from some kind of structural disorder (Löffler & Mader 2003), which certainly weakens the elasticity constants, and is very likely the reason for the observed dilatation of the corundum lattice in precipitates embedded in the rutile matrix.

Let us now take a closer look at the unusual appearance of the dislocations appearing on both sides of the corundum precipitates. The dislocations are formed in the hosting rutile lattice and are often pinned at the surface steps of the corundum particle, as demonstrated in the HRTEM image in Figure 5d. The structural mismatch between an ideal rutile and corundum lattice is shown in Figure 5e, where ½ of the Vernier period of the misfit is shown. The good fitting region is at the bottom, where the A-type oxygen plane of the corundum meets an A-type oxygen plane of rutile, whereas at the top, there is the most unfavorable situation, where A-type oxygen plane of corundum meets a B-type oxygen plane of rutile. Therefore, the dislocations are located there, and typical for dislocations in the vicinity of the dislocation core are the bent lattice planes in corundum as well as in the rutile. In the study of Gao *et al*. (1992) as well as in the present

work, the Burgers vector of the misfit dislocations has a length corresponding to the nearest distance between closed-packed oxygen layers, or between the nearest distance of two metal ions. In rutile this is the length of the *a*-axis, *i.e.*, the Burgers vector here is $\boldsymbol{b} = [010]_R$, and the misfit dislocations have a pure edge character. However, such a large Burgers vector will produce large stressed and strains in the crystal, as the energy associated with the dislocation scales with b^2 (Hirth and Lothe 1992). The unusual character of the misfit dislocations at the corundum-rutile interface is schematically explained in Figure 6. As often observed in *fcc* metals, vacancies condense at close-packed planes and produce vacancy loops bounded by the edge dislocations as shown in Fig. 6a. More complex and wider loops may dissociate into partials with shorter Burgers vectors according to $\boldsymbol{b} = \boldsymbol{b}_1 + \boldsymbol{b}_2$ to reduce the strain energy (Fig. 6b). In our case we observe periodically arranged dislocations in rutile surrounding the corundum particle. These dislocations are dissociated into partials $\boldsymbol{b}_1 = ½\cdot[111]_R$ and $\boldsymbol{b}_2 = ½\cdot[\bar{1}1\bar{1}]_R$ (Fig. 6c). Between the partial dislocations a stacking fault is generated where the atomic arrangement of the crystal periodicity is interrupted at the stacking fault plane (Fig. 6d). The somewhat structurally disordered planar regions in the rutile crystal in Figure 5d are therefore interpreted as stacking faults. Partial dislocation $\boldsymbol{b}_1$ is located right at the corundum-rutile interface, usually at a surface step. It may be written as $\boldsymbol{b}_1 = ½\cdot[111]_R = ½\cdot[010]_R + ½\cdot[101]_R$, where the first component is a shift to bring *e.g.*, an oxygen B-plane to an A-plane position, which then fits to an oxygen A-plane of corundum, whereas the second component of $\boldsymbol{b}_1$ represents a displacement normal to the interface. To avoid problems with the corundum crystal, it appears very reasonable that partial $\boldsymbol{b}_1$ is located at an interface step where some degree of structural disorder exists anyway. Partial dislocation $\boldsymbol{b}_2$ is located in the rutile matrix *ca*. 10 nm away from the corundum-rutile interface, at the other end of the stacking fault. The first component of partial $\boldsymbol{b}_2 = ½\cdot[\bar{1}1\bar{1}]_R = ½\cdot[010]_R + ½\cdot[\bar{1}0\bar{1}]_R$ is the same as that of $\boldsymbol{b}_1$, and together they compensate for the lattice misfit between the corundum and the rutile. The second component of $\boldsymbol{b}_2$ has the function to compensate for the shift of the partial $\boldsymbol{b}_1$ normal to the interface so that the misfit dislocation $\boldsymbol{b}$ becomes a pure edge dislocation. These planes are seen edge-on in Figure 5d, running horizontal in the drawing (Fig. 6d).

Discussion

The formation of precipitates through exsolution from parent crystals, often involving a sequence of temperature-dependent phase transformations, is an important indicator of past geochemical processes (Boudeulle 1994). The exsolution and precipitation processes are a consequence of supersaturation of the existing solid solution. The excess solute is excreted finding the easiest possible structural relation with the parent crystal. To reconstruct the sequence of these unknown transient processes, detailed structural and chemical characterization of the precipitate–matrix relations is of great help. Here, the origin of the corundum precipitates appears to be a key for understanding the course of the reactions during the crystallization of rutile. The expansion of the corundum lattice, the apparent porosity of the corundum precipitates, their clustering at the primary twin boundary, and the presence of secondary twins, in their own way reflect the geochemical processes associated with the genesis of (101) twins in rutile, as discussed in the following.

Rutile–corundum epitaxial relationship

The observed epitaxial relationship of rutile and corundum is well known from other studies. The same epitaxial relations have been reported for Ti-rich blue sapphire, displaying a 6-fold asterism, which is caused by numerous precipitates of rutile coherently intergrown within the corundum crystals (Phillips *et al.* 1980a, Phillips *et al.* 1980b). To reduce the strain induced by the tetragonal deformation of rutile, the precipitates grow as {101} twins. Through twinning, the deformation of the O-sublattice is brought to a minimum at the $\{11\bar{2}0\}_C \parallel \{101\}_R$ interfaces. In Ti-supersaturated synthetic α-Al_2O_3 the formation of submicron precipitates of high-pressure α-TiO_2 polymorph was reported (Jayaram 1988), which were related to the twinning of rutile in star corundum (Moon & Phillips 1991; Xiao *et al.* 1997; He *et al.* 2011). There are only a few studies of corundum precipitation in rutile. In Al-doped rutile, the formation of nanosized corundum precipitates was reported (Bursill & Blanchin 1989; Blanchin & Bursill 1989). While the epitaxial relationship between the two phases is consistent with the one reconstructed on α-Al_2O_3 precipitates at (101) twin boundaries in the rutile of our study, there, in contrast, no twinning of rutile was observed. Interest-

ingly, however, the authors reported the rhombohedral twinning of corundum, which took place to accommodate the residual lattice strains.

Based on the previous studies there is no direct implication that the twinning of rutile could be induced by the precipitation of corundum. Therefore we may anticipate that a process other than just the exsolution of excess Al precedes the twin formation. Most indicative for such process are the expansion of the basal planes in corundum and the related larger distance between the misfit dislocations and the lamellar-pore structure observed in the corundum precipitates. Such features are not observed in those corundum precipitates that formed in Al-supersaturated rutile (Bursill & Blanchin 1989, Blanchin & Bursill 1980) and moreover, the distance between the misfit dislocations along the $(11\bar{2}0)_C \parallel (101)_R$ interfaces viewed in the $[1\bar{1}00]_C \parallel [10\bar{1}]_R$ projections are always close to the predicted value of D = 7.53 nm. For example, in epitaxial films of rutile on $(11\bar{2}0)_C$ substrates, Gao *et al*. (1992) reported that the films were perfectly coherent in the $[0001]_C \parallel [010]_R$ orientation; however, when the films were viewed in the $[1\bar{1}00]_C \parallel [10\bar{1}]_R$ projection they observed series of misfit dislocations at an average distance of D = ~8.0 nm. In another work by He *et al.* (2011), who studied the structure of interfaces on rutile precipitates in Ti-supersaturated corundum, they showed a slightly larger distance between the misfit dislocations D = ~8.2 nm in this projection. Both values are significantly lower than ours (D = ~11.5 $\pm$ 1.1 nm), indicating that the studied rutile crystals did not originally grow on corundum, but on some other, structurally related precursor, and that corundum is not a primary mineral phase.

The origin of corundum precipitates in rutile

The question remains – if not corundum, what could then be the original precursor for the growth of rutile, and what triggers the twinning? In the study of (301) twins in rutiles from this locality Daneu *et al.* (2007) found that the (301) twins formed by the epitaxial growth of rutile on an Fe-Ti-Al oxyhydroxide precursor with the tivanite-type structure, and in the process of dehydration, the tivanite transforms to Al-rich ilmenite. As (101) twins of rutile are commonly found in (sagenite) clusters together with the (301) twins, it

is reasonable to assume that they also formed by replacement and epitaxial growth on some Al-rich oxyhydroxide precursor. Recently Grey *et al*. (2010) described an Al-rich hydroxylian pseudorutile (HPR) from Indonesia with a tivanite-type structure that contains numerous up to 10 nm large precipitates of diaspore (α-AlOOH). The hexagonal anion sublattice of Al-rich HPR (a = 0.2845 nm, c = 0.4574), matches the anion sublattice of rutile surprisingly well, and as such it could be an ideal precursor for the crystallization of rutile during dehydration at elevated temperatures, as described by Daneu *et al.* (2007), while in the same process diaspore would be transformed into corundum (Löffler & Mader 2003).

In the study of diaspore–corundum dehydration Löffler & Mader (2003) reported that in this process the a, b and c axes of the diaspore are translated into the c, $[11\bar{2}0]_C$ and $[1\bar{1}00]_C$ axes of corundum, which is consistent with the orientation of the precipitates in our samples. Namely, if the corundum–rutile interface relationship $[1\bar{1}00]_C(11\bar{2}0)_C \parallel [10\bar{1}]_R(101)_R$, as observed at our (101) twin interfaces, is translated into a diaspore–rutile interface we obtain the relationship $[001]_D(040)_D \parallel [10\bar{1}]_R(101)_R$. Using the temperature dependence data of diaspore (Hill 1979; Löffler & Mader 2003) and rutile (Henderson *et al*. 2009) we can calculate the distance between the misfit dislocations for such a hypothetical diaspore–rutile interface. The obtained values ($D \approx$ 10–11 nm) are consistent with the measured distances in our precipitates. Moreover, at ~400°C the $(100)_D$ = 0.4418 nm spacing of the diaspore (Löffler & Mader 2003) matches the $(0003)'_C$ lattice spacings of our corundum precipitates, implying their close relation to the diaspore. Such an unusual expansion of corundum may be a consequence of the rearrangement of Al atoms in the preexisting O-sublattice, which has been fixed by the preceding rutile–diaspore relation. Furthermore, this suggests that the O-sublattice remains largely unaltered after the diaspore-to-corundum transformation. To some extent the dilatation may also be stabilized by the incorporation of Ti atoms, as indicated by our EDS analysis of the precipitates. On dehydration of the diaspore at temperatures above 400°C a typical lamellar-pore structure of corundum is formed, which is a result of a large volume decrease of -28 % during the transformation (Löffler & Mader 2003). A similar pore-structure was observed in all our corundum precipitates. This observation additionally confirms that prior to dehydration into corundum the precipitates were originally diaspore.

The characteristic distance between the misfit dislocations and the porosity of corundum suggests that the precipitates nucleated as diaspore within rutile matrix at temperatures around ~400°C and consequently dehydrated to corundum at elevated temperatures. While the observed expansion of the corundum lattice along the crystallographic *c*-axis can be explained by the spatial confinement of precipitates within the preexisting rutile matrix, this on the other hand induced considerable residual strains, causing deformations in the surrounding rutile lattice (Takeuchi & Hashimoto 1990). As a consequence of the strains caused by the dehydration of diaspore, secondary {101} twin-pairs formed in the vicinity of the precipitates.

Nucleation mechanism of (101) rutile twins from Diamantina

Based on the understanding of the origin of corundum precipitates, we can reconstruct the processes that took place during the formation of (101) twins of rutile at the Diamantina locality. In the first stage of replacement, the surface of Al-rich HPR starts to dehydrate at elevated temperatures under oxidizing conditions. As a result, Ti^{4+} ions within the pseudorutile O-sublattice are rearranged to form rutile, while the excess H_2O diffuses through the pore channels along the rutile *c*-axis (Sasaki *et al.* 1985). In addition to replacement, rutile also crystallizes on the surface of the HPR template from Ti^{4+}-rich solutions and grows in an euhedral shape, characteristic for rutile. The tivanite, *i.e.* pseudorutile structure, offers a common framework for two different arrangements of Ti atoms, leading to single or twinned rutile orientations (Grey & Nickel 1981; Daneu *et al.* 2007). Hence a twin will be formed if at any point of the primary HPR crystal rutile starts to nucleate in different orientation. As the incidence of both arrangements is identical, the probability of the nucleation of domains in a twinned orientation increases with the increasing number of nucleation points on the surface of the primary HPR crystal. As soon as one crystallization pattern is assumed, it continues to grow all the way to the central point of the precursor crystal, producing either a single crystal or a twin. During the progressive crystallization of rutile all the impurity ions diffuse towards the interior of the HPR crystal. As their concentration exceeds the solubility limit, the impurities are excreted in the form of discrete phases. This happens in the case of Al-rich HPR, where aluminum has a very low solu-

bility limit in rutile (Bromiley & Hilairet 2005). As a result, the excess Al-oxyhydroxide precipitates in the form of diaspore. When the clusters reach a certain critical size their diffusivity (*i.e.*, mobility) becomes lower than the rate of rutile growth and consequently, the precipitates become occluded by the hosting crystal. Diaspore precipitates, reported in Al-rich hydroxylian pseudorutile by Grey *et al.* (2010), are smaller than our precipitates. The larger size of our precipitates is likely to be a consequence of a snowball effect at the progressive crystallization front of the rutile until the critical mass is reached and the precipitates are overgrown (*see* illustration in Figure 7). While some of the diaspore particles are overgrown by rutile as they reach the critical size, the larger part of the Al-rich oxyhydroxides is being flushed towards the centre of the precursor crystal. In the final stage of HPR dehydration two oppositely growing rutile domains meet at the centre of the precursor HPR crystal, forming a twin boundary, which acts as a natural obstacle for the mobility of the Al-oxyhydroxide clusters. This could explain why the majority of the precipitates are concentrated at the primary (101) twin boundary. In the final stage of recrystallization the boundary between the two domains is gradually equilibrated into a straight twin boundary following the lowest-energy (101) interface plane. During late stages of dehydration, the diaspore particles finally transform to corundum, which leads to a volume decrease and causes tensions in the surrounding rutile. The strains caused by the dehydration of the diaspore precipitates are compensated by the formation of parallel {101} twin boundaries, which are according to Takeuchi and Hashimoto (1990) the easy direction for strain relaxation in rutile. Meanwhile, more rutile is being deposited on the crystal surfaces forming a characteristic V-shaped twin morphology in the orientation predetermined in by the initial HPR replacement. The mechanism of the genesis of (101) twins of rutile is illustrated in Figure 7.

Genesis of multiple-twinned sagenite networks of rutile

Given the fact that in Diamantina {101} twins of rutile are found in sagenite-like clusters together with {301} twins, we propose a united mechanism for their formation. In the study of (301) twins from the same locality Daneu *et al*. (2007) suggested that they form by the dehydration of an Al-rich (Fe,Ti)-oxyhydroxide precursor having a multiple-twinned tivanite-type structure (Grey & Nickel 1983) in the temperature range

386 300-400°C, which is a similar temperature range as determined in this work. The formation of both types of
387 twins appears to be associated with the exsolution of corundum-type phases: (*i*) *ilmenite* segregates to
388 {301} planes of rutile (Daneu *et al*. 2007), whereas (*ii*) *corundum* segregates to {101} planes of rutile (this
389 work). If we take a closer look at the orientation relationship between ilmenite and rutile $[0001]_I(1\bar{1}00)_I \parallel$
390 $[010]_R(301)_R$, and between corundum and rutile $[0001]_C(11\bar{2}0)_C \parallel [010]_R(101)_R$, we realize that only the in-
391 terface is different, while the orientation of the corundum-type phase and the rutile remain identical. This
392 strongly suggests that both types of twins nucleated from the same precursor mineral, as illustrated in Fig-
393 ure 8.

394 Rutile and corundum-type minerals as well as the related oxyhydroxides, possess a common oxygen
395 sublattice, enabling fast and effective mineral replacement processes (Putnis 2009). Al-rich hydroxylian
396 pseudorutile (HPR; kleberite) recently reported by Grey *et al*. (2010) and Grey *et al*. (2013), which compris-
397 es rutile-type, goethite-type and diaspore-type structural elements. Such an Al-rich HPR also seems to be
398 the most likely precursor in our case. The process of dehydration of pseudorutile associated with water
399 loss, the exsolution of Fe^{3+}-ions, and the replacement by rutile is known as leucoxenization (Ignatiev 1999).
400 On dehydration of the precursor phase, Ti^{4+}-ions are reorganized within a common oxygen framework to
401 form a rutile structure. Rutile can principally crystallize in three possible directions with its *c*-axes rotated
402 by 120° within the oxygen sublattice of the precursor phase, which are due to tetragonal deformation of
403 rutile further split into two variants of each principal orientation, yielding 6 unique *c*-axis orientations. De-
404 pending on the coincidence of rutile domains we obtain a set of different rutile–rutile interfaces forming
405 impressive sagenite networks of reticulated rutile crystals, among which the {101} and {301} twin bounda-
406 ries are most prominent (Armbruster 1981). In principle, all these interfaces are produced by accidental
407 impingement of oppositely growing rutile domains.

408 While no dopant seems to be necessary for the formation of any of these interfaces, including the twin
409 boundaries, we observe an interface-specific segregation of impurity elements, which implies that in the fi-
410 nal stage of interface equilibration these elements have a decisive role on the type of the interface formed

between the two domains. The segregation of $Fe^{3+}$and Al^{3+} ions appears to be strongly related with the genesis of {301} and {101} twins of rutile, respectively. This can be substantiated by structural matching between the rutile and different corundum-type and tivanite-type phases crystallizing within a common *hcp* oxygen sublattice, as shown in Table I. A simple lattice misfit calculation (Equation 1) shows that the best fit for the (101)-twin is obtained with Al-rich phases (diaspore and corundum) whereas for the (301)-twin with the Fe-rich phases (tivanite, goethite, ilmenite and hematite) indicating that the lattice match determines which phase will segregate to the specific twin boundary. While the parent mineral that is the precursor for the formation of reticulated twins in Diamantina appears to be Al-rich HPR, it is possible that any other structurally related mineral (listed in Table I) could serve as a template for the twinning of rutile on other localities.

Implications

Investigations of the twinning in minerals represents a fundamental scientific challenge that offers possibilities for a true understanding of the basic building principles of solids and the initial stages of phase transformations in minerals. Unlike in other minerals, *e.g.* sphalerite (Šrot *et al.* 2003), spinel (Daneu *et al.* 2007) or bixbyite (Kleebe & Lauterbach 2008), where special (twin) boundaries are triggered by the presence of a specific impurity element, which initiates faulted stacking in the crystal's nucleation stage, twining in rutile appears to be more complex. We have shown that the formation of {101} and {301} twins in rutile is not only chemically induced, but is a result of the topotaxial replacement of an oxyhydroxide precursor.

The nanostructural analysis of corundum precipitates segregated on the (101) twin boundary in rutile implied that they are remnants of past transient processes involving the dehydration of a parent Al-rich hydroxylian pseudorutile phase, which served as a precursor for rutile crystallization at elevated temperatures. While the twinned orientation is accomplished by the random nucleation of rutile on the surface of the precursor, the actual interface is equilibrated depending on the structural matching of the exsolved impurity phase with rutile lattice. In the case of ilmenite exsolution the interface is {301} (Daneu *et al.* 2007) whereas in the case of corundum the preferred interface is the {101} of rutile (present work). Once the interface is established, the rest of the crystal grows in a predetermined orientation forming a characteristic twin morphology. For the first time, a unified mechanism for the formation of sagenitic rutile clusters was proposed.

The unusual complexity of twinning in rutile presented in this work demonstrates that the formation of twins in natural minerals is chemically triggered and is not a result of the accidental coalescence of crystals in the nucleation stage. Studying the origin of twinning in natural minerals at the nanometer scale helps to reconstruct the dynamics of geochemical processes during the time of their formation.

Acknowledgments

This work was supported under the research grant No. 3-7121-SLO/1119347 by the Alexander von Humboldt (AvH) foundation. The financial support of the Slovenian Ministry for Science under the project No. J1-4167-1555-04 is also gratefully acknowledged.

References

Abrahams, S.C. and Berstein, J.L. (1971) Rutile: Normal probability plot analysis and accurate measurement of crystal structure. The Journal of Chemical Physics, 55, 3206-3211.

Armbruster, T. (1981) On the origin of sagenites: Structural coherency of rutile with hematite and spinel structure types. Neues Jahrbuch für Mineralogie, 7, 328-334.

Blake, R.L., Hessevick, R.E., Zoltai, T and Finger, L.W. (1966) Refinement of the hematite structure. American Mineralogist, 51, 123-129.

Blanchin, M.G. and Bursill, L.A. (1989) Non-classical twinning of alumina precipitates in rutile. Philosophical Magazine A, 60, 619-630.

Boudeulle, M. (1994) Disproportionation in mineral solid solutions: Symmetry constraints on precipitate orientation and morphology. Implications for the study of oriented intergrowths. Journal of Applied Crystallography, 27, 567-573.

Brumiley, G.D. and Hilairet, N. (2005) Hydrogen and minor element incorporation in synthetic rutile. Mineralogical Magazine, 69, 345-358.

Bursill, L.A. and Blanchin, M.G. (1989) Interphase structures observed as alumina precipitates in rutile. Philosophical Magazine A, 60, 631-642.

Daneu, N., Rečnik, A., Yamazaki, T. and Dolenec, T. (2007) Structure and chemistry of (111) twin boundaries in $MgAl_2O_4$ spinel crystals from Mogok. Physics and chemistry of minerals, 24, 233-247.

Daneu, N., Schmid, H., Rečnik, A. and Mader, W. (2007) Atomic structure and formation mechanism of (301) rutile twins from Diamantina (Brazil). American Mineralogist, 92, 1789-1799.

Force, E.R., Richards, R.P., Scott, K.M., Valentine, P.C. and Fishman, N.S. (1996) Mineral intergrowths replaced by »elbow-twinned« rutile in altered rocks. Canadian Mineralogist, 34, 605-614.

Gao, Y, Merkle, K.L., Chang H.L., Zhang, T.J. and Lam, D.J. (1992) Study of defects and interfaces on the atomic scale in epitaxial TiO_2 thin films on sapphire. Philosophical Magazine, 65, 1103-1125.

Grey, I.E. and Nickel, E.H. (1981) Tivanite, a new oxyhydroxide mineral from Western Australia, and its structural relationship to rutile and diaspore. American Mineralogist, 66, 866–871.

Grey, I.E., Bordet, P., Wilson, N.C., Townend, R., Bastow, T.J. and Brunelli, M. (2010) A new Al-rich hydroxylian pseudorutile from Kalimantan, Indonesia. American Mineralogist, 95, 161-170.

Grey, I.E., Steinike, K. and MacRae, C.M. (2013) Kleberite, $Fe^{3+}Ti_6O_{11}(OH)_5$, a new ilmenite alteration product, from Königshain, northeast Germany. Mineralogical Magazine, 77, 45-55.

He J., Lagerlof, K.P.D. and Heuer, A.H. (2011) Structural evolution of TiO_2 precipitates in Ti-doped sapphire (α-Al_2O_3). Journal of the American Ceramic Society, 94, 1272-1280.

Hill, R.J. (1979) Crystal structure refinement and electron density distribution in diaspore. Physics and Chemistry of Minerals, 5, 179-200.

Hirth, J.P. and Lothe, J. (1992) Theory of Dislocations, Krieger Publishing Company, Malabar: Florida, USA.

Ignatiev, V.D. (1999) Solid-phase mechanism of the ilmenite leucoxenization. Lithology and Mineral Resources, 34, 184-189.

Janssen, A., Putnis, A., Geisler, T. and Putnis, C.V. (2010) The experimental replacement of ilmenite by rutile in HCl solutions. Mineralogical Magazine, 74, 633-644.

Jayaram, V. (1988) The precipitation of alpha-TiO_2 from supersaturated solutions of Ti in alumina (Crystal structure and morphology). Philosophical Magazine A, 57, 525-542.

Kirfel, A. and Eichhorn, K. (1990) Accurate structure analysis with synchrotron radiation - the electron density in Al_2O_3. Acta Crystallographica A, 46, 271-284.

Kleebe, H.J. and Lauterbach, S. (2008) Exaggerated grain growth in bixbyite via fast diffusion along planar defects. Crystal Research and Technology, 43, 1143-1149.

Li, G.L., Wang, G.H. and Hong, J.M. (1999) Morphologies of rutile form TiO_2 twins crystals. Journal of Materials Science Letters, 18, 1243-1246.

Lima-de-Faria, J. (1963) Dehydration of goethite and diaspore. Zeitschrift für Kristallographie, 119, 176-203.

Löffler, L. and Mader, W. (2003) Transformation mechanism of the dehydration of diaspore. Journal of the American Ceramic Society, 86, 534-540.

Lu, W., Bruner, B., Casillas, G., He, J., Jose-Yacaman, M. and Farmer, P.J. (2012) Large scale synthesis of V-shaped rutile twinned nanorods. CrystEngComm, 14, 3120-2124.

Moon, A.R. and Phillips, M.R. (1991) Titania precipitation in sapphire containing iron and titanium. Physics and Chemistry of Minerals, 18, 251-258.

Penn, R.L. and Banfield, J.F. (1998) Oriented attachment and growth, twinning, polytypism, and formation of metastable phases: Insights from nanocrystalline TiO_2. American Mineralogist, 83, 1077-1082.

Phillips, D.S., Heuer, A.H. and Mitchell, T.E. (1980) Precipitation in star sapphire – I. Identification of the precipitate. Philosophical Magazine A, 42, 385-404.

Phillips, D.S., Heuer, A.H. and Mitchell, T.E. (1980) Precipitation in star sapphire – II. Elastic accommodation of the precipitate. Philosophical Magazine A, 42, 405-416.

Putnis, A. (2009) Mineral replacement reactions. Reviews in Mineralogy & Geochemistry, 70, 87-124.

Reece, M. and Morell, R. (1991) Electron microscope study of non-stoichiometric titania. Journal of Materials Science, 26, 5566-5574.

Sasaki, J., Peterson, N.L. and Hoshino, K. (1985) Tracer impurity diffusion in single-crystal rutile (TiO_{2-x}). Journal of Physics and Chemistry of Solids, 46, 1267-1283.

Suzuki, K., Ichinara, M. and Takeuchi, S. (1991) High-resolution electron microscopy of lattice defects in TiO_2 and SnO_2. Philosophical Magazine A, 63, 657-665.

519 Šrot, V., Rečnik, A., Scheu, C., Šturm, S. and Mirtič, B. (2003) Stacking faults and twin boundaries in
520 sphalerite crystals from the Trepča mines in Kosovo. American Mineralogist, 88, 1809-1816.

521 Takeuchi, S. and Hashimoto, T. (1990) Deformation mechanism in titanium dioxide single crystals. Journal
522 of Materials Science, 25, 417-423.

523 Wechsler B A. and Prewitt C.T. (1984) Crystal structure of ilmenite ($FeTiO_3$) at high temperature and at high
524 pressure. American Mineralogist, 69, 176-185.

525 Xiao, S.Q., Dahmen, U. and Heuer, A.H. (1997) Phase transformation of TiO_2 precipitates in sapphire (α-
526 Al_2O_3) induced by the loss of coherency. Philosophical Magazine A, 75, 221-238.
527

528 **List of Figure captions**

529

530 **Figure 1**: (**a**) Perfectly developed (101) twin of rutile from Diamantina region, Brazil. (101) twin boundary divides
531 the crystal into two symmetric twin domains with the characteristic angle of 114.4° between the crystallographic c-
532 axes. Many planar faults parallel to {101} planes are visible in the central part of the crystal. (**b**) A schematic drawing
533 of (101) twin with indicated [010] and [10$\bar{1}$] projections for TEM specimen preparation.

534

535 **Figure 2**: FEG-SEM/BSE image of the surface of the TEM specimen, prepared close to the $[010]_R$ zone axis, contain-
536 ing (101) twin boundary at the centre. The twin domains are made visible through channeling effects, where lattice
537 planes of domain I are in better alignment with respect to the incident electron beam than those of domain II. The
538 main (101) twin is characterized by a series of tiny black inclusions lined along the twin interface. EDS analysis re-
539 vealed that these inclusions contain aluminum. Secondary (101) twins, which are visible in the right twin domain, typi-
540 cally contain fewer Al-rich inclusions. Waviness of the surface results from ion-milling of the specimen.

541

542 **Figure 3**: (**a**) Bright-field (BF) TEM image of parallel {101} twin boundaries in rutile viewed along [010] projection
543 with an inset showing a dark-field (DF) image produced with a (10$\bar{1}$) reflection. (**b**-**d**) SAED patterns from the areas
544 marked in (a) show that crystal domains across the interfaces are in twin orientation. The DF image is produced with a
545 reflection from domain I, marked in (c), and consequently domain II appears dark. (**e**) HRTEM image of a single (101)
546 twin boundary (TW; highlighted red) with a simple structural model, as proposed by Takeuchi and Hashimoto (1990).

547

548 **Figure 4**: TEM study of primary (101) twin of rutile in $[010]_R$ projection. (**a**) BF-TEM image showing 150 nm large
549 lenticular precipitate located at the main twin boundary. (**b**) SAED pattern, recorded form the area marked in the TEM
550 image, reveals a fine orientation relationship between the rutile and the precipitate. Additional reflections (indicated
551 by arrows) correspond to corundum in $[0001]_C$ projection. (**c**) Schematic pattern of (101) twin of rutile with superim-
552 posed corundum reflections. (**d**) HRTEM image of the corundum – rutile interface with a structural model of thin co-
553 rundum interlayer at the $(101)_R$ twin interface.

554

555 **Figure 5**: TEM study of the primary (101) twin boundary of rutile in $[10\bar{1}]_R$ projection. (**a**) Low-magnification TEM
556 image showing four evenly distributed α-Al_2O_3 precipitates lined along the primary twin interface. The inset in the
557 lower right corner shows a detail of corundum precipitate with uniformly spaced misfit dislocations extending ~10 nm

into the hosting rutile lattice. (**b**) SAED pattern shows additional reflections corresponding to $[1\bar{1}00]_C$ (marked by arrows). (**c**) Schematic reciprocal space pattern of superimposed rutile twin and corundum reflections. All reflections from the two rutile domains (I and II) are common. (**d**) HRTEM image of (101) twin boundary (TW) in rutile with semi-coherent corundum precipitate. Extended misfit dislocations in rutile, marked by red arrows, are pinned to surface steps. The misfit is compensated in rutile lattice by two partial dislocations, $\boldsymbol{b}_1$ and $\boldsymbol{b}_2$, separated by a stacking fault (SF). Pores in corundum are a common feature. (**e**) Corundum–rutile interface showing structural mismatch of the two lattices in the $[1\bar{1}00]_C$ or $[10\bar{1}]_R$ projection from an ideal match (bottom) to the largest mismatch where an oxygen A-type layer faces the oxygen B-type layer across the interface (top). This distance roughly corresponds to half-the-distance between the two misfit dislocations observed in the experimental images.

Figure 6. Dissociation of misfit dislocations as observed at the corundum-rutile interface. (**a**) A simple vacancy loop in *fcc* metals. (**b**) Due to the AB stacking of oxygen planes in rutile $\boldsymbol{b} = [010]_R$ it is split into two partial dislocations $\boldsymbol{b}_1$ and $\boldsymbol{b}_2$. (**c**) Simple vacancy loops in rutile with $\boldsymbol{b} = [010]_R$ surrounding a corundum particle and (**d**) misfit dislocations $\boldsymbol{b} = [010]_R$ dissociated into $\boldsymbol{b}_1$ and $\boldsymbol{b}_2$ separated by a stacking fault (SF). The $\boldsymbol{b}_1$ is usually pinned at the interface step of corundum, whereas $\boldsymbol{b}_2$ is located at the other end of the SF.

Figure 7. Genesis of (101) twins from Diamantina, based on nanoscale structural analysis of the specimens. Their formation involves three stages: (*i*) dehydration of Al-rich hydroxylian pseudorutile (HPR), (*ii*) primary twin formation and growth and (*iii*) dehydration of diaspore and the formation of secondary parallel twin pairs. In the first stage, rutile starts to replace the primary (Ti, Al)-oxyhydroxide mineral through its dehydration and diffusion of Ti^{4+} ions into the hosting structure, while on the surface, rutile grows epitaxially following the structural pattern defined by the initial rutile orientation. During dehydration, Ti-dominated oxyhydroxide is converted into rutile, while Al gets excreted in form of minute diaspore nanoparticles on the crystallization front. When Al-rich domains become too large for diffusional drifting through permeable tivanite-type structure, they become occluded. In the course of replacement two rutile domains eventually meet at the centre of originating oxyhydroxide, forming a twin boundary, where the majority of diaspore particles are collected. With elevated temperature, corundum is formed in place of diaspore as the final dehydration product. To compensate lattice strains after dehydration secondary twins are formed in rutile.

Figure 8. Schematic presentation of the formation of (101) and (301) rutile twins on Al-rich hydroxylian pseudorutile (HPR) precursor (Grey *et al.* 2010). In the beginning of the dehydration process, rutile starts to crystallize from the Al-rich HPR with a tivanite-type structure. Rutile nucleates on the surface of the precursor and progressively

replaces this primary mineral. Depending on the coincidence of oppositely growing rutile domains (101) and (301) twins can be formed. Due to tetragonal distortion of rutile, (Fe,Ti)-rich oxyhydroxide (pseudorutile) will be preferably segregated to {301} planes, whereas Al-rich oxyhydroxide (diaspore) better matches the {101} planes of rutile (*see* Table 1). In the final stage of dehydration the remaining oxyhydroxides are converted to oxides, ilmenite and corundum. Resulting orientation relationship for ilmenite–rutile interface is $[0001]_I(1\bar{1}00)_I \parallel [010]_R(301)_R$, and that for corundum – rutile is $[0001]_C(11\bar{2}0)_C \parallel [010]_R(101)_R$. Note that the orientation of rutile and the precipitated corundum-type layer stays identical, only the interface is different. For simplicity, a common hexagonal oxygen framework is assumed.

Tables

Table I. Calculated misfit (δ) and distance between misfit dislocations (D) between rutile and some phases related by common *hcp* oxygen sublattice: diaspore, corundum, Al-rich HPR, (Fe,Ti)-tivanite, goethite, ilmenite and hematite. The lattice match is calculated (Eq. 1) for both twin interfaces in $[010]_R \parallel [0001]_{hcp}$ projection using d-spacings of the planes running normal to the interface (⊥ plane). Larger the D distance, better the match between the two lattices.

		Rutile	Diaspore	Corundum	Al-rich HPR	Tivanite	Goethite	Ilmenite	Hematite
(101) twin	⊥ plane	$\frac{1}{2}\sqrt{a^2+c^2}$	$\frac{1}{2}b_D/\sqrt{3}$	$a_C/\sqrt{3}$	$\frac{1}{2}c_{HPR}/\sqrt{3}$	$\frac{1}{2}c_T/\sqrt{3}$	$\frac{1}{2}b_G/\sqrt{3}$	$a_I/\sqrt{3}$	$a_H/\sqrt{3}$
	d-spacing	0.2732 nm	0.2717 nm	0.2746 nm	0.2845 nm	0.2888 nm	0.2869 nm	0.2934 nm	0.2909 nm
	δ [%]	N/A	**0.6**	**0.5**	4.1	5.6	4.9	7.1	6.3
	D [nm]	N/A	49.5	53.6	6.9	5.1	5.7	4.0	4.5
(301) twin	⊥ plane	$\frac{1}{2}\sqrt{a^2+3c^2}$	$\frac{1}{2}b_D$	a_C	$\frac{1}{2}c_{HPR}$	$\frac{1}{2}c_T$	$\frac{1}{2}b_G$	a_I	a_H
	d-spacing	0.4997 nm	0.4706 nm	0.4757 nm	0.4927 nm	0.5003 nm	0.4975 nm	0.5088 nm	0.5038 nm
	δ [%]	N/A	6.0	4.9	**1.4**	**0.1**	**0.4**	**1.8**	**0.8**
	D [nm]	N/A	8.1	9.9	35.2	416.7	113.0	27.9	61.4

References for cell parameters (including their standard deviations) at room temperature: Rutile – Abrahams and Bernstein (1971); Diaspore – Hill (1979); Corundum – Kirfel and Eichhorn (1990); Al-rich HPR – Grey *et al.* (2010); Tivanite – Grey and Nickel (1981); Goethite – Lima-de-Faria (1963); Ilmenite – Wechsler and Prewitt (1984) and Hematite – Blake *et al*. (1966). Standard deviations of the calculated δ and D values are 3-4 orders of magnitude below the significant figures listed in the Table.

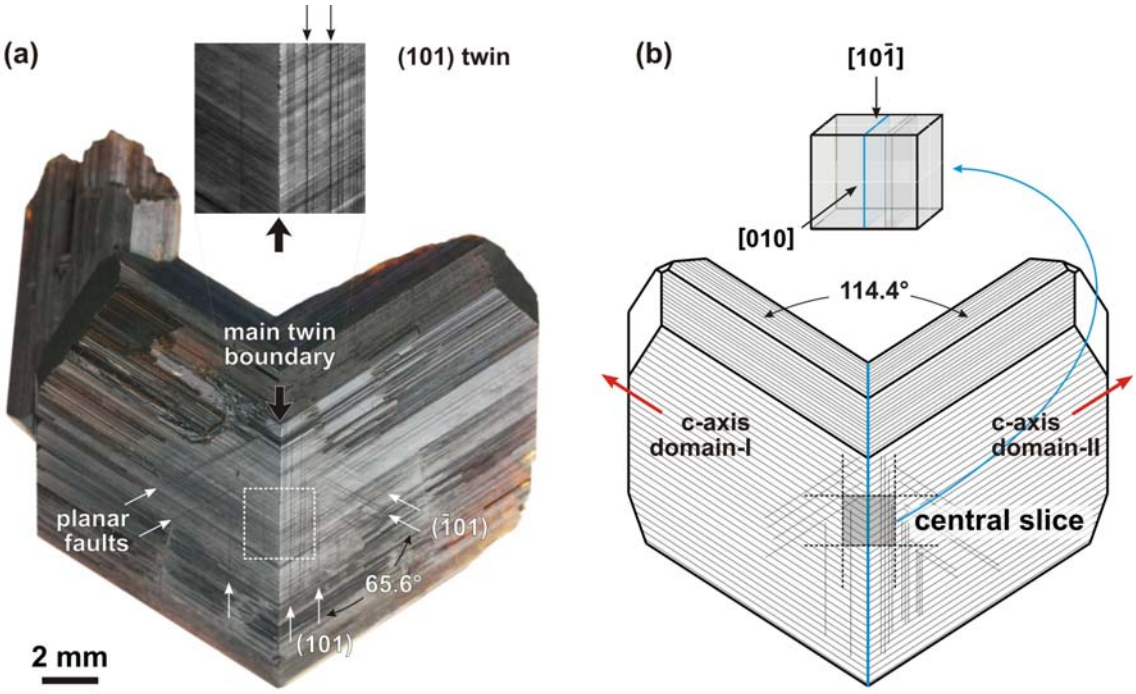

Figure 1: (**a**) Perfectly developed (101) twin of rutile from Diamantina region, Brazil. (101) twin boundary divides the crystal into two symmetric twin domains with the characteristic angle of 114.4° between the crystallographic c-axes. Many planar faults parallel to {101} planes are visible at central part of the crystal. (**b**) A schematic drawing of (101) twin with indicated [010] and [10$\bar{1}$] projections for TEM specimen preparation.

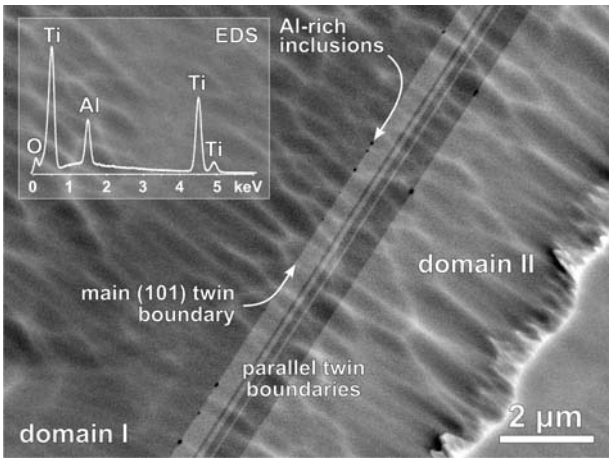

Figure 2: FEG-SEM/BSE image of the surface of the TEM specimen, prepared close to the $[010]_R$ zone axis, containing (101) twin boundary at the centre. The twin domains are made visible through channeling effects, where lattice planes of domain I are in better alignment with respect to the incident electron beam than those of domain II. The main (101) twin is characterized by a series of tiny black inclusions lined along the twin interface. EDS analysis revealed that these inclusions contain aluminum. Secondary (101) twins, which are visible in the right twin domain, typically contain less Al-rich inclusions. Waviness of the surface results from ion-milling of the specimen.

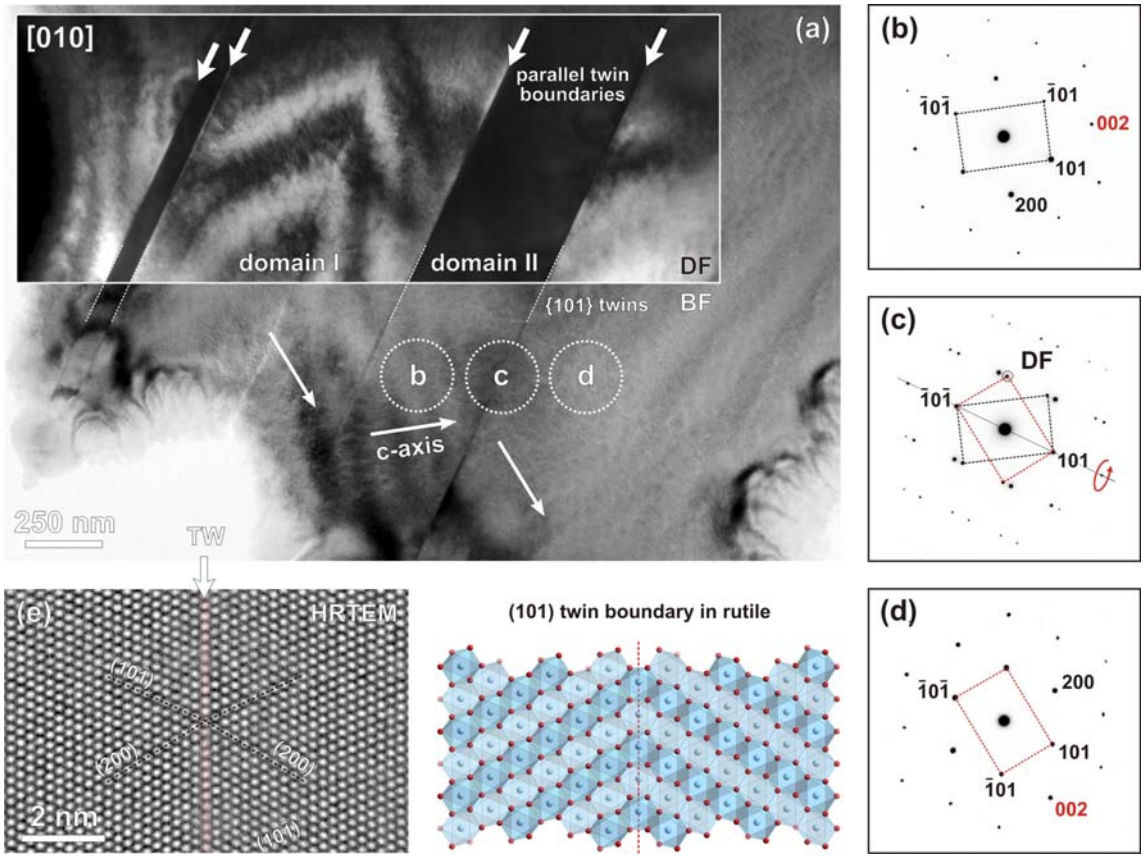

Figure 3: (**a**) Bright-field (BF) TEM image of parallel {101} twin boundaries in rutile viewed along [010] projection with an inset showing a dark-field (DF) image produced with a (10$\bar{1}$) reflection. (**b**-**d**) SAED patterns from the areas marked in (a) show that crystal domains across the interfaces are in twin orientation. The DF image is produced with a reflection from domain I, marked in (c), and consequently domain II appears dark. (**e**) HRTEM image of a single (101) twin boundary (TW; highlighted red) with a simple structural model, as proposed by Takeuchi and Hashimoto (1990).

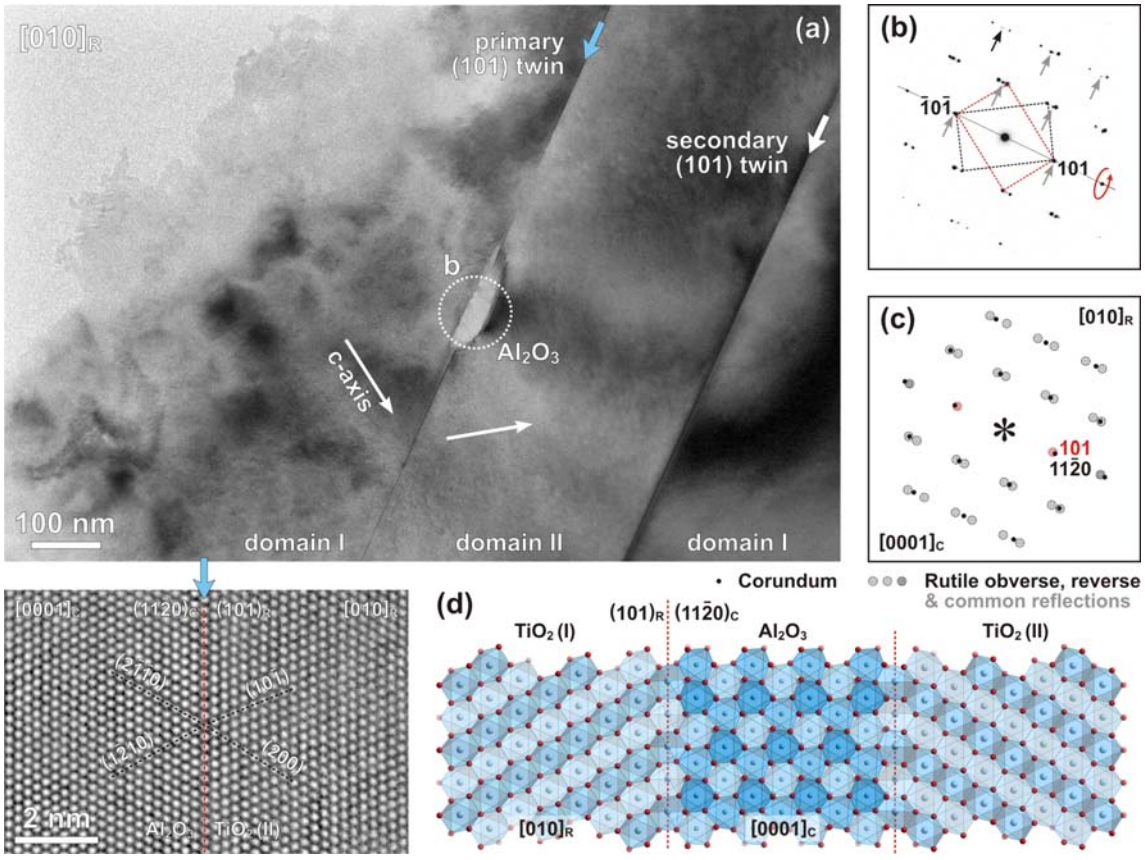

Figure 4: TEM study of primary (101) twin of rutile in $[010]_R$ projection. (**a**) BF-TEM image showing 150 nm large lenticular precipitate located at the main twin boundary. (**b**) SAED pattern, recorded form the area marked in the TEM image, reveals a fine orientation relationship between the rutile and the precipitate. Additional reflections (indicated by arrows) correspond to corundum in $[0001]_C$ projection. (**c**) Schematic pattern of (101) twin of rutile with superimposed corundum reflections. (**d**) HRTEM image of the corundum – rutile interface with a structural model of thin corundum interlayer at the $(101)_R$ twin interface.

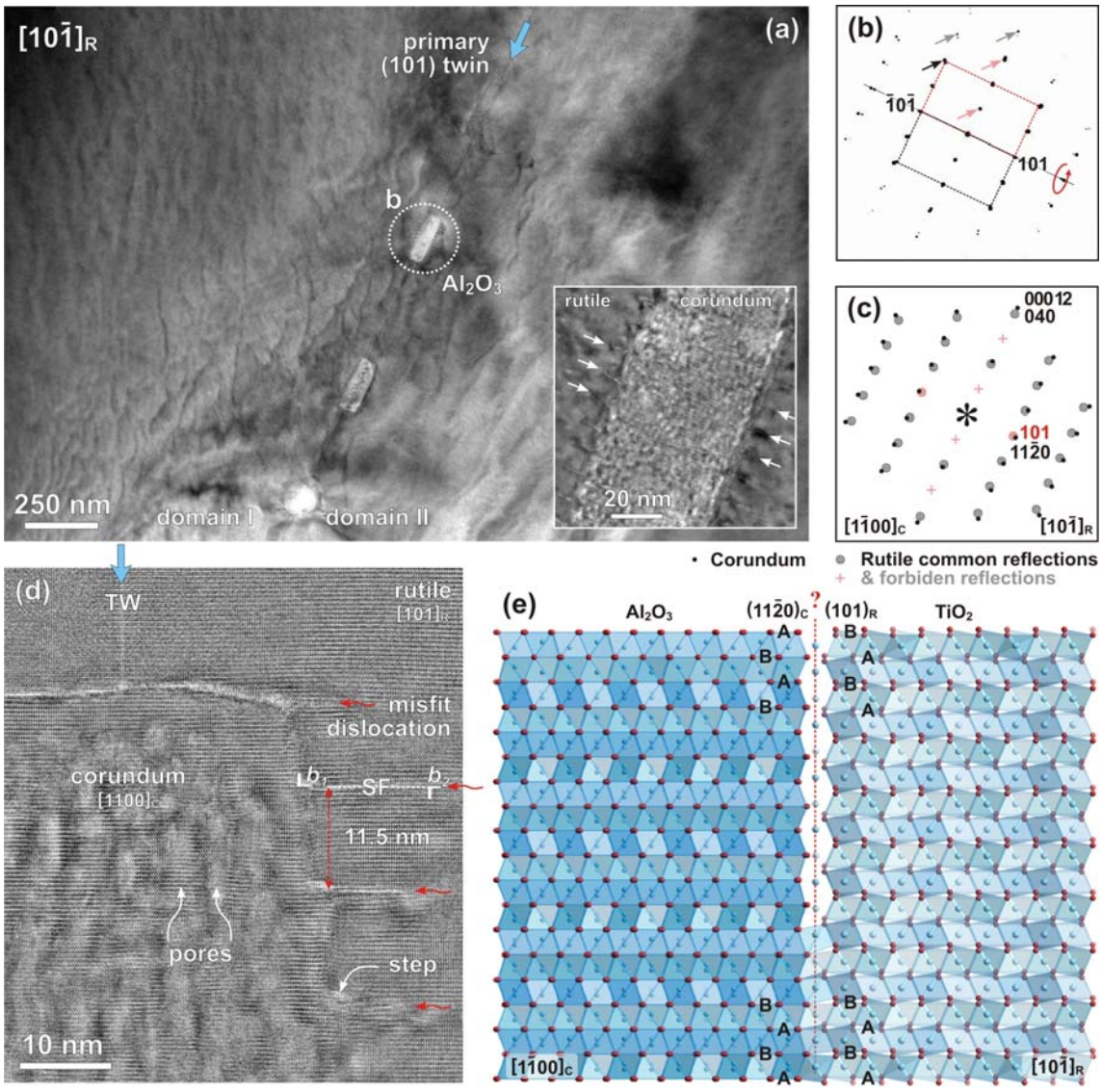

Figure 5: TEM study of the primary (101) twin boundary of rutile in $[10\bar{1}]_R$ projection. (**a**) Low-magnification TEM image showing four evenly distributed α-Al_2O_3 precipitates lined along the primary twin interface. The inset in the lower right corner shows a detail of corundum precipitate with uniformly spaced misfit dislocations extending ~10 nm into the hosting rutile lattice. (**b**) SAED pattern shows additional reflections corresponding to $[1\bar{1}00]_C$ (marked by arrows). (**c**) Schematic reciprocal space pattern of superimposed rutile twin and corundum reflections. All reflections from the two rutile domains (I and II) are common. (**d**) HRTEM image of (101) twin boundary (TW) in rutile with semi-coherent corundum precipitate. Extended misfit dislocations in rutile, marked by red arrows, are pinned to surface steps. The misfit is compensated in rutile lattice by two partial dislocations, $\boldsymbol{b}_1$ and $\boldsymbol{b}_2$, separated by a stacking fault (SF). Pores in corundum are a common feature. (**e**) Corundum – rutile interface showing structural mismatch of the two lattices in the $[1\bar{1}00]_C$ or $[10\bar{1}]_R$ projection from an ideal match (bottom) to the largest mismatch where an oxygen A-type layer faces the oxygen B-type layer across the interface (top). This distance roughly corresponds to half-the-distance between the two misfit dislocations observed in the experimental images.

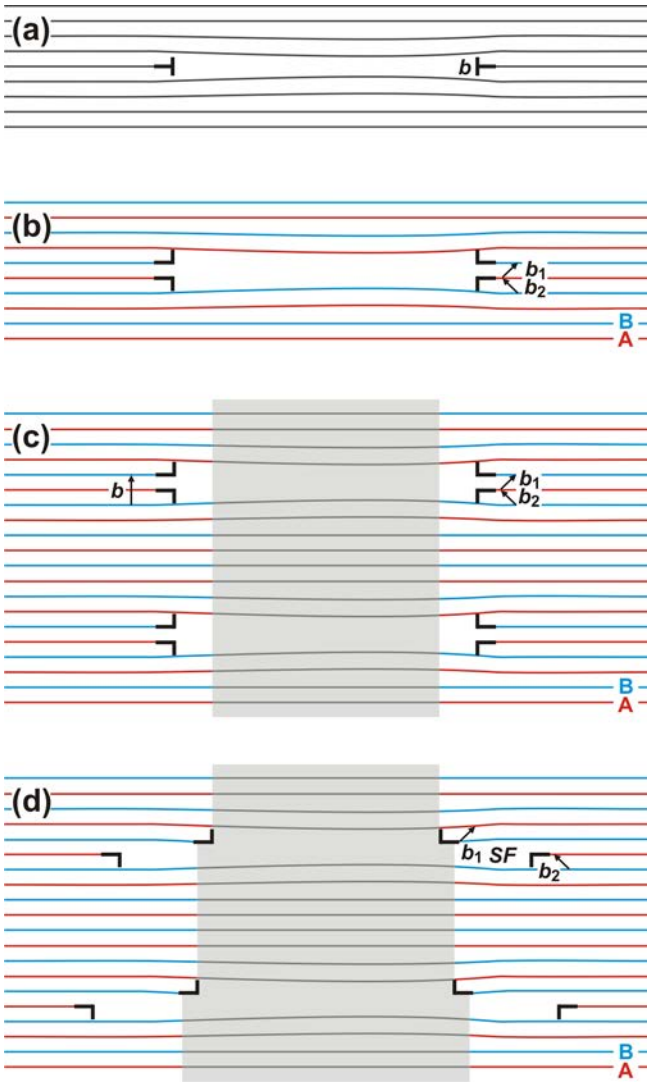

Figure 6. Dissociation of misfit dislocations as observed at the corundum-rutile interface. (**a**) A simple vacancy loop in *fcc* metals. (**b**) Due to the AB stacking of oxygen planes in rutile $\boldsymbol{b} = [010]_R$ it is split into two partial dislocations $\boldsymbol{b}_1$ and $\boldsymbol{b}_2$. (**c**) Simple vacancy loops in rutile with $\boldsymbol{b} = [010]_R$ surrounding a corundum particle and (**d**) misfit dislocations $\boldsymbol{b} = [010]_R$ dissociated into $\boldsymbol{b}_1$ and $\boldsymbol{b}_2$ separated by a stacking fault (SF). The $\boldsymbol{b}_1$ is usually pinned at the interface step of corundum, whereas $\boldsymbol{b}_2$ is located at the other end of the SF.

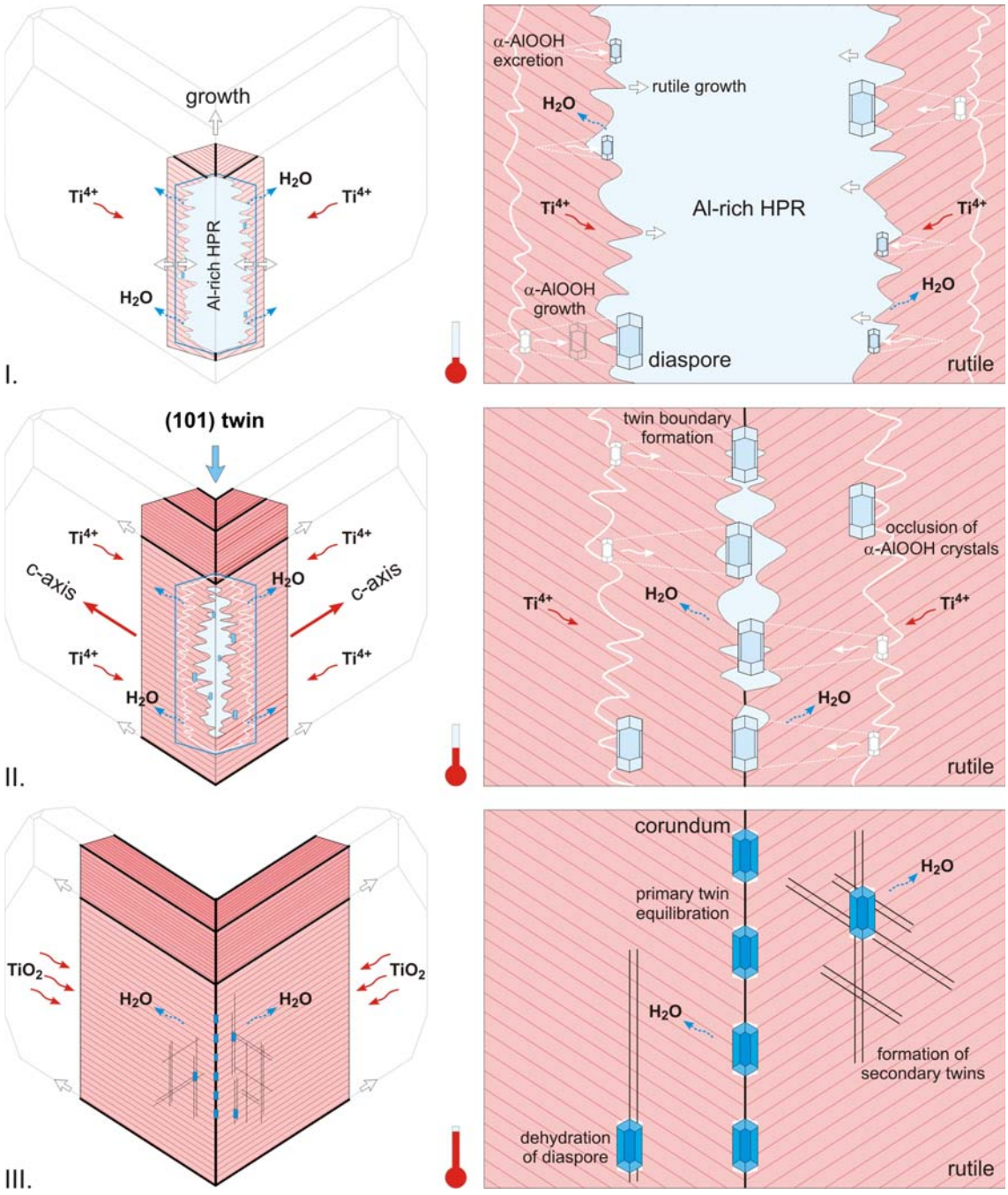

Figure 7. Genesis of (101) twins from Diamantina, based on nanoscale structural analysis of the specimens. Their formation involves three stages: (*i*) dehydration of Al-rich hydroxylian pseudorutile (HPR), (*ii*) primary twin formation and growth and (*iii*) dehydration of diaspore and the formation of secondary parallel twin pairs. In the first stage, rutile starts to replace the primary (Ti, Al)-oxyhydroxide mineral through its dehydration and diffusion of Ti^{4+} ions into the hosting structure, while on the surface, rutile grows epitaxially following the structural pattern defined by the initial rutile orientation. During dehydration, Ti-dominated oxyhydroxide is converted into rutile, while Al gets excreted in form of minute diaspore nanoparticles on the crystallization front. When Al-rich domains become too large for diffusional drifting through permeable tivanite-type structure, they become occluded. In the course of replacement two rutile domains eventually meet at the centre of originating oxyhydroxide, forming a twin boundary, where the majority of diaspore particles are collected. With elevated temperature, corundum is formed in place of diaspore as the final dehydration product. To compensate lattice strains after dehydration secondary twins are formed in rutile.

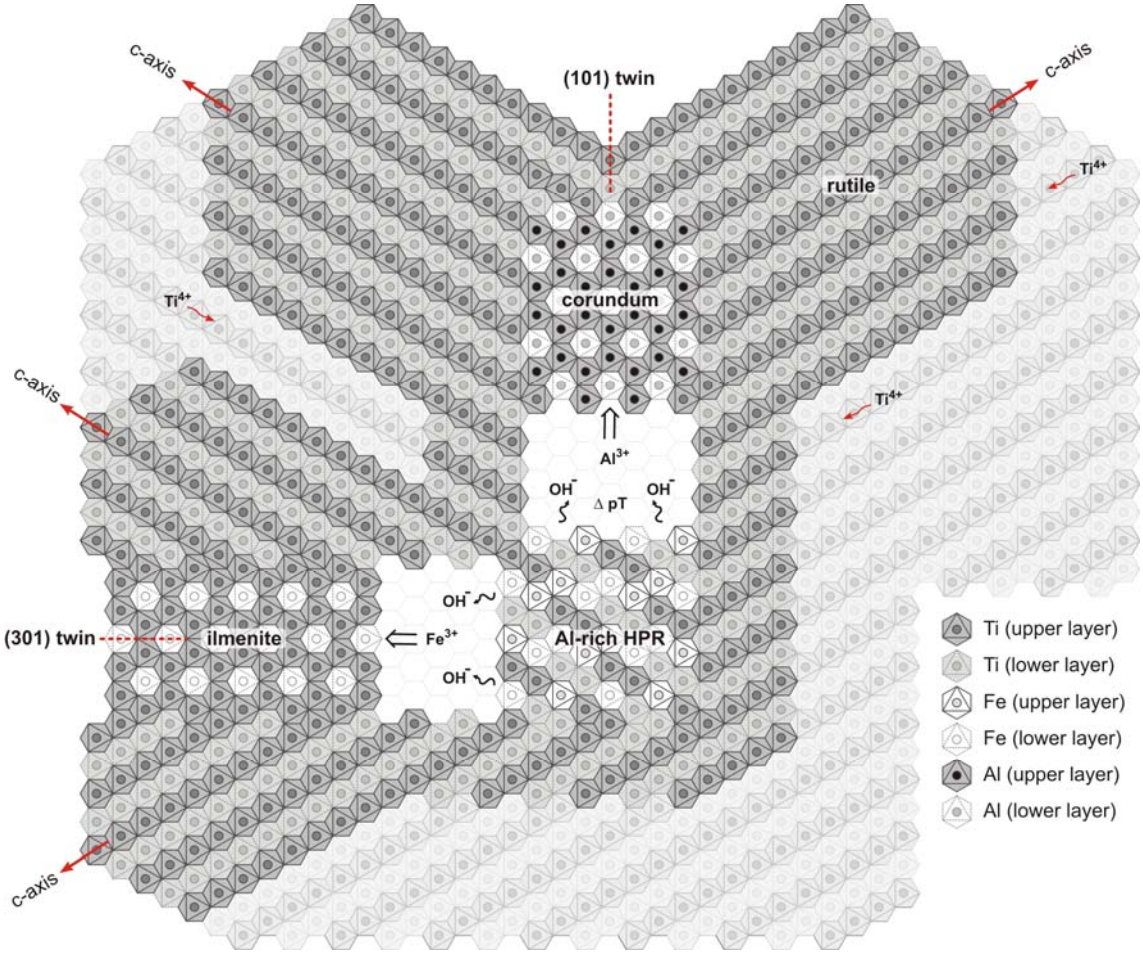

Figure 8. Schematic presentation of the formation of (101) and (301) rutile twins on Al-rich hydroxylian pseudorutile (HPR) precursor (Grey *et al.* 2010). In the beginning of the dehydration process, rutile starts to crystallize from the Al-rich HPR with a tivanite-type structure. Rutile nucleates on the surface of the precursor and progressively replaces this primary mineral. Depending on the coincidence of oppositely growing rutile domains (101) and (301) twins can be formed. Due to tetragonal distortion of rutile, (Fe,Ti)-rich oxyhydroxide (pseudorutile) will be preferably segregated to {301} planes, whereas Al-rich oxyhydroxide (diaspore) better matches the {101} planes of rutile (*see* Table 1). In the final stage of dehydration the remaining oxyhydroxides are converted to oxides, ilmenite and corundum. Resulting orientation relationship for ilmenite – rutile interface is $[0001]_I(1\bar{1}00)_I \parallel [010]_R(301)_R$, and that for corundum – rutile is $[0001]_C(11\bar{2}0)_C \parallel [010]_R(101)_R$. Note that the orientation of rutile and the precipitated corundum-type layer stays identical, only the interface is different. For simplicity, a common hexagonal oxygen framework is assumed.

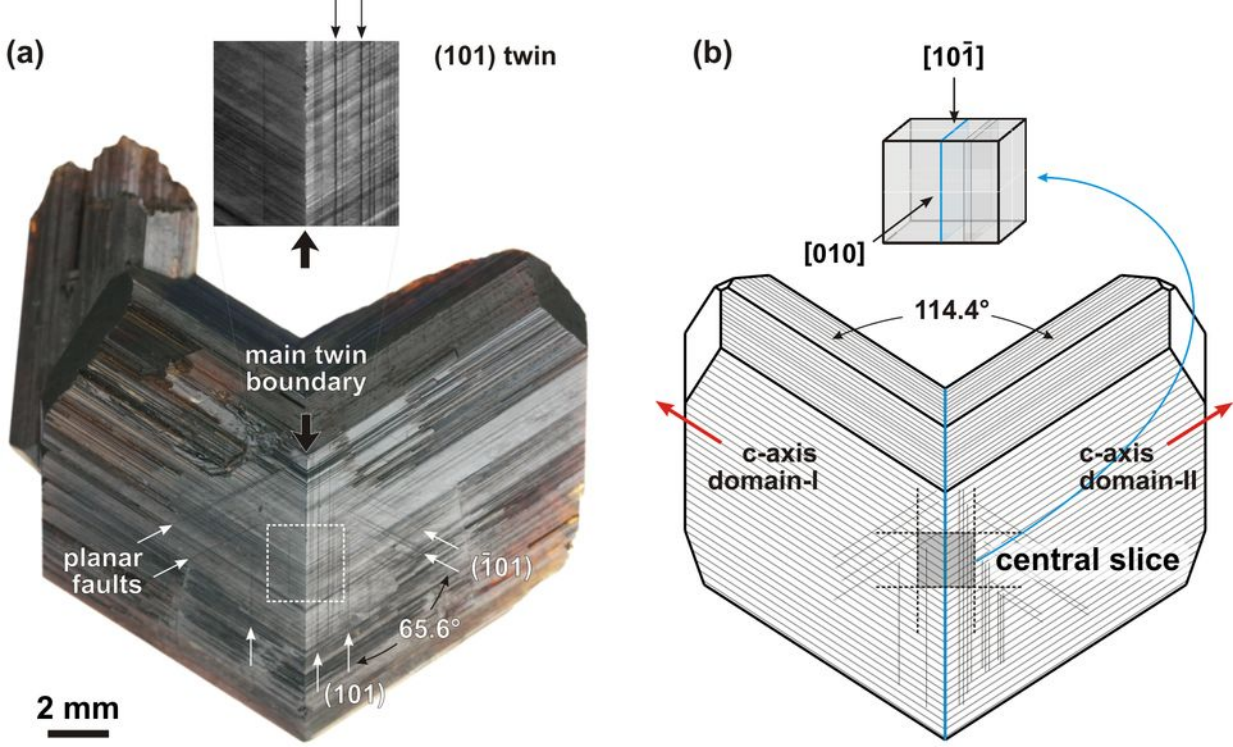
(a)
(101) twin
main twin boundary
planar faults
(1̄01)
65.6°
(101)
2 mm
(b)
[101̄]
[010]
114.4°
c-axis domain-I
c-axis domain-II
central slice

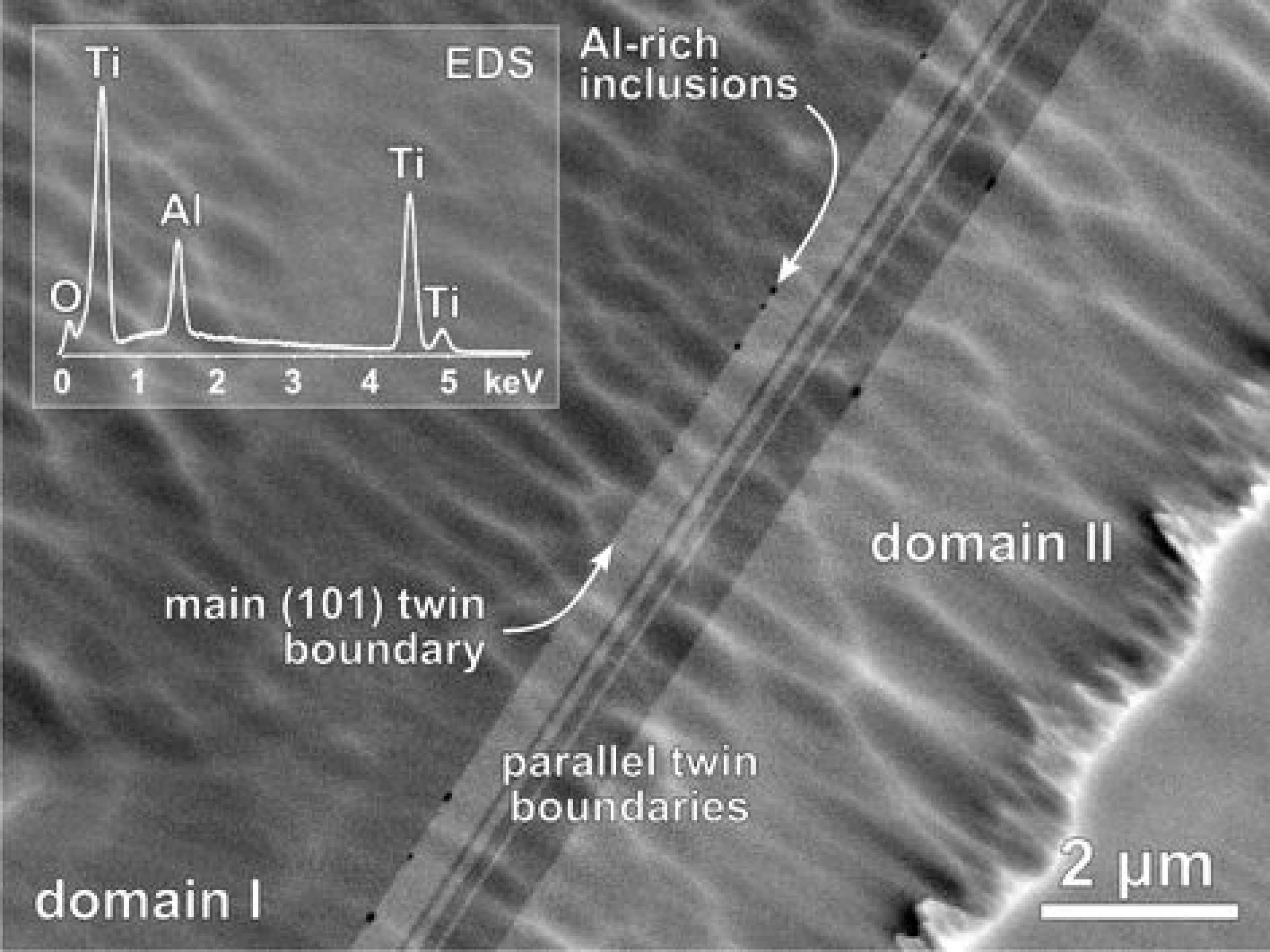
Ti
EDS
Al
Ti
O
Ti
0 1 2 3 4 5 keV
Al-rich
inclusions
domain II
main (101) twin
boundary
parallel twin
boundaries
2 μm
domain I

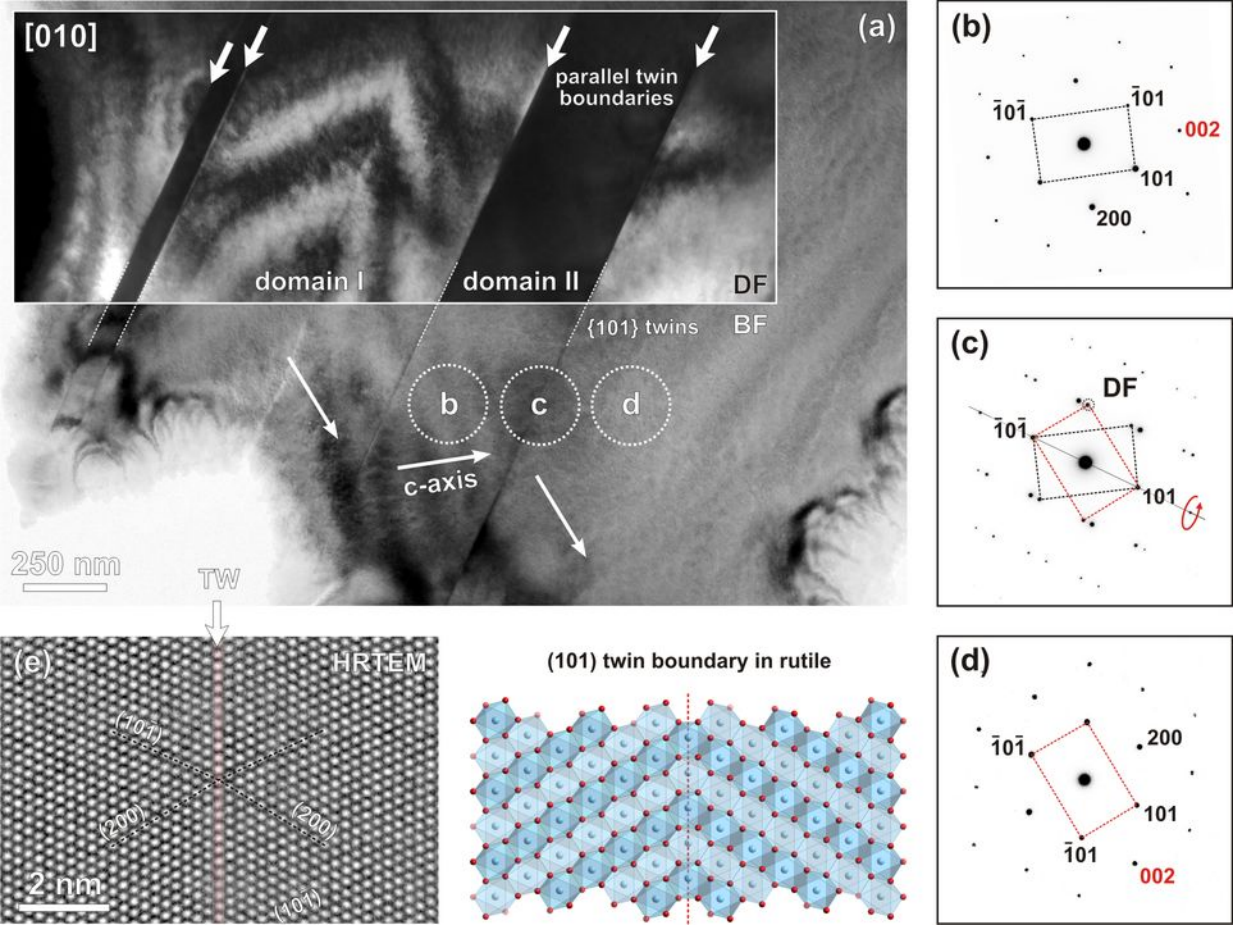
[010]
(a)
parallel twin boundaries
domain I
domain II
DF
BF
{101} twins
b
c
d
c-axis
250 nm
TW
(b)
$\bar{1}01$
$\bar{1}01$
002
101
200
(c)
DF
$\bar{1}01$
101
(d)
$\bar{1}01$
200
101
$\bar{1}01$
002
(e)
HRTEM
(101)
(200)
(200)
(10$\bar{1}$)
2 nm
(101) twin boundary in rutile

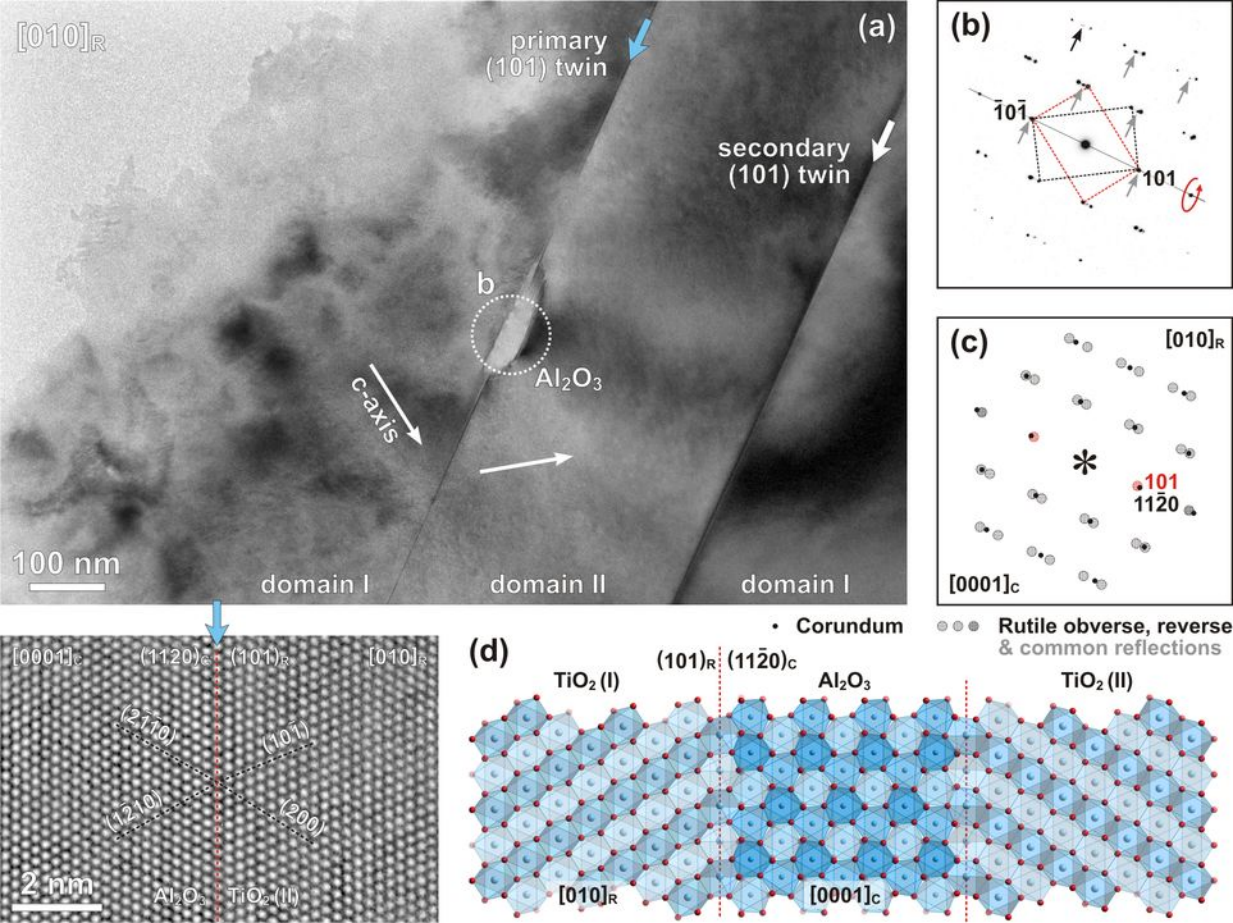
[010]R
primary
(101) twin
(a)
secondary
(101) twin
b
Al2O3
c-axis
100 nm
domain I
domain II
domain I
(b)
101
101
(c)
[010]R
*
101
11$\bar{2}$0
[0001]C
[0001]C
(11$\bar{2}$0)C
(10$\bar{1}$1)R
[010]R
(2$\bar{1}$$\bar{1}$0)
(10$\bar{1}$1)
(11$\bar{2}$0)
(200)
2 nm
Al2O3
TiO2 (II)
• Corundum
Rutile obverse, reverse
& common reflections
(d)
TiO2 (I)
(101)R
(11$\bar{2}$0)C
Al2O3
TiO2 (II)
[010]R
[0001]C

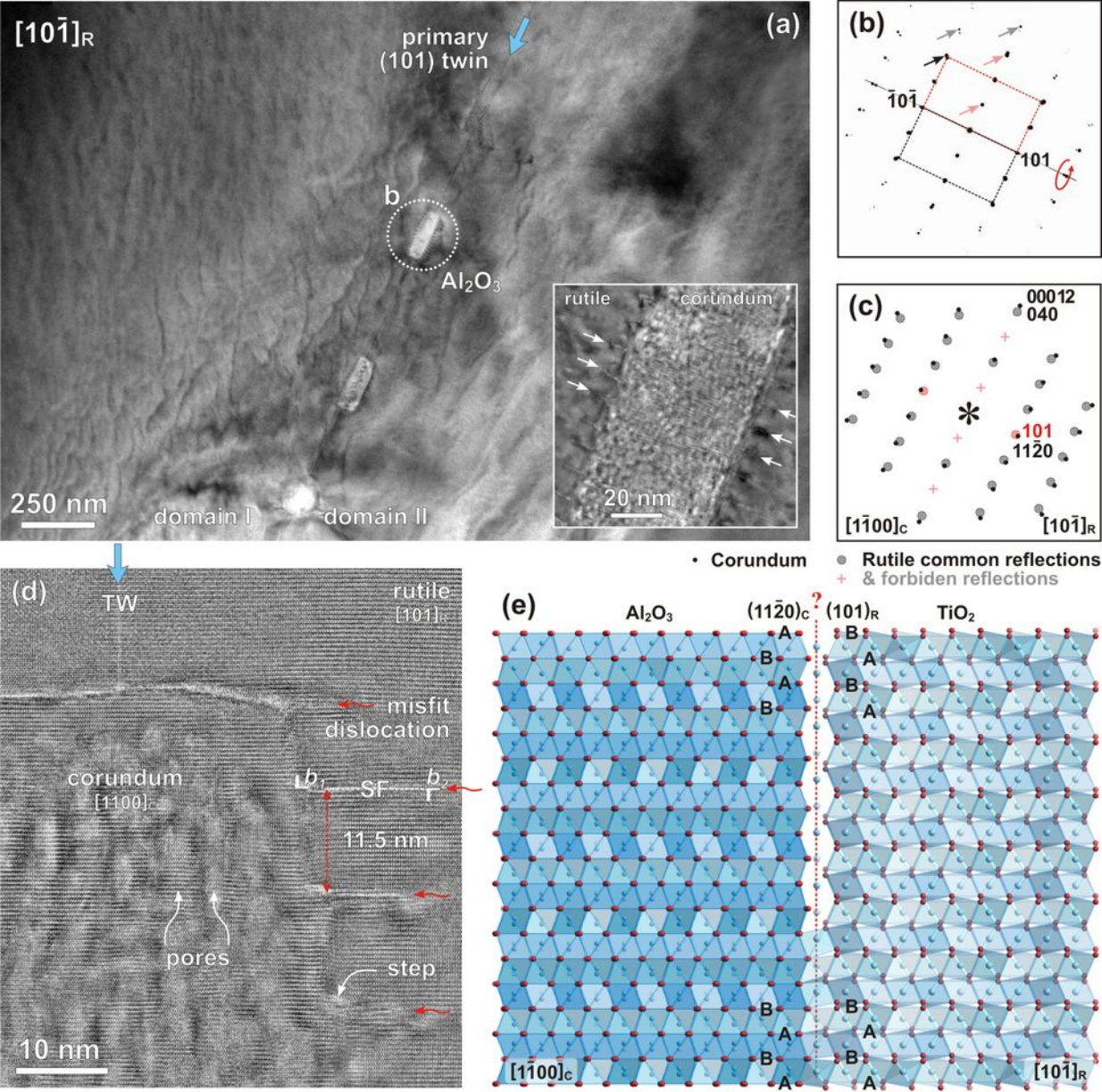
[10$\bar{1}$]$_R$
primary
(101) twin
(a)
b
Al_2O_3
rutile
corundum
20 nm
250 nm
domain I
domain II
(b)
$\bar{1}$01
101
(c)
00012
040
101
11$\bar{2}$0
[1$\bar{1}$00]$_C$
[10$\bar{1}$]$_R$
• Corundum
Rutile common reflections
& forbiden reflections
(d)
TW
rutile
[101]$_R$
misfit
dislocation
corundum
[1100]$_C$
b_1
SF
b_2
11.5 nm
pores
step
10 nm
(e)
Al_2O_3
(11$\bar{2}$0)$_C$
(101)$_R$
TiO_2
A
B
[1$\bar{1}$00]$_C$
[10$\bar{1}$]$_R$

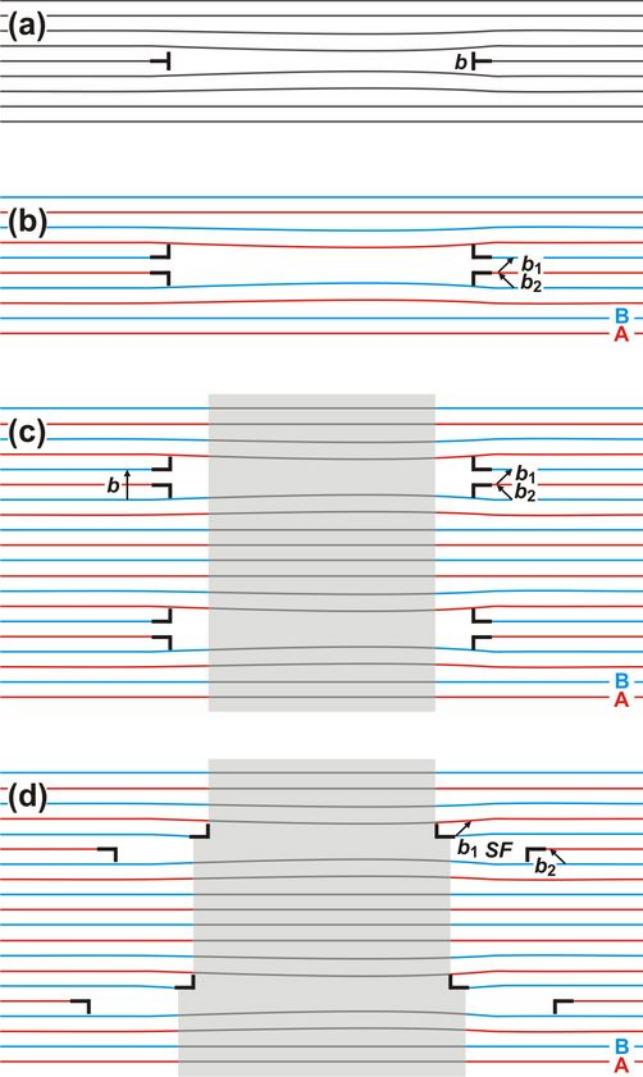
(a)
b
(b)
b1
b2
B
A
(c)
b
b1
b2
B
A
(d)
b1 SF
b2
B
A

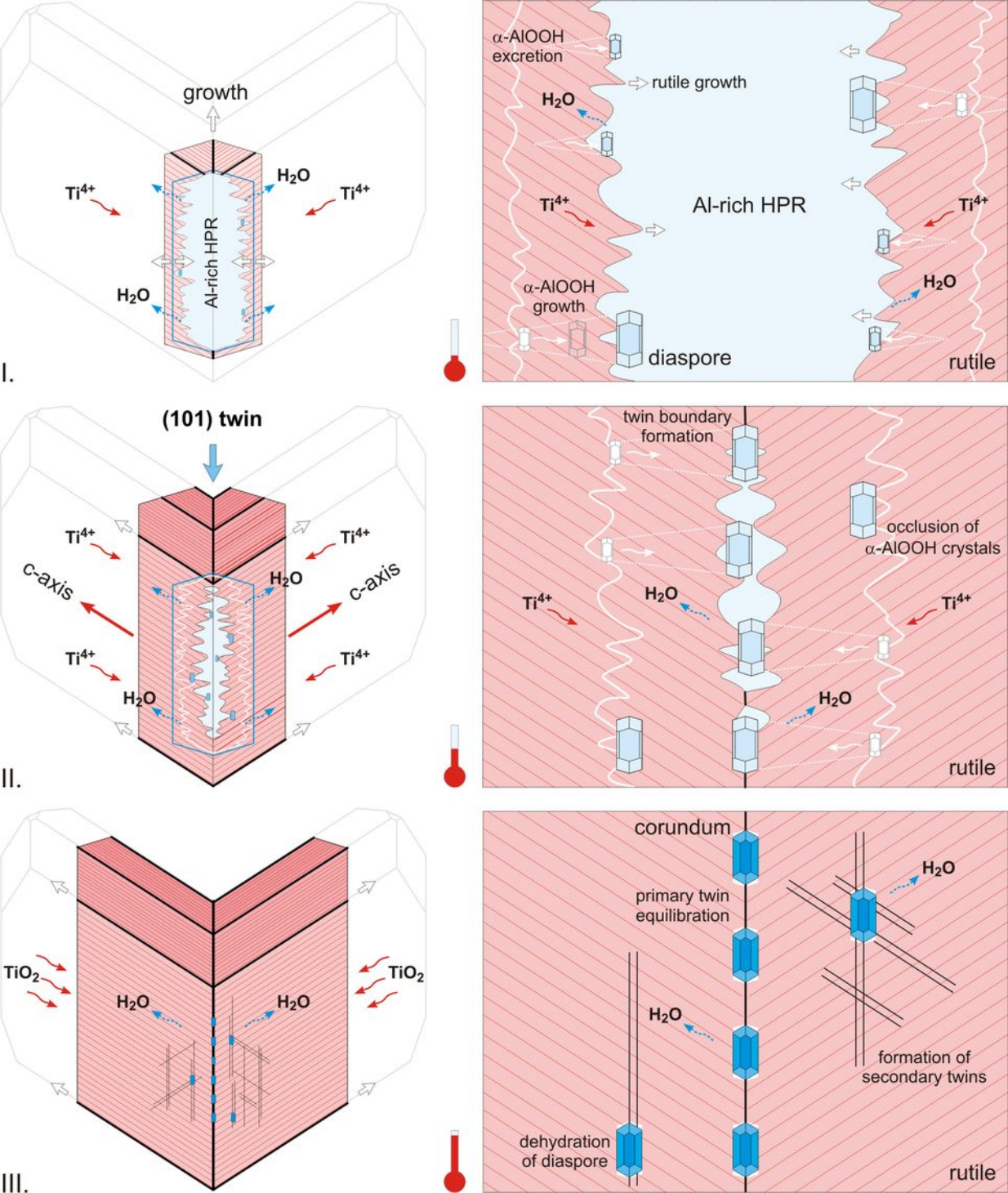
I.
growth
Ti4+
H2O
Ti4+
Al-rich HPR
H2O
α-AlOOH
excretion
rutile growth
H2O
Ti4+
Al-rich HPR
Ti4+
H2O
α-AlOOH
growth
diaspore
rutile
II.
(101) twin
Ti4+
Ti4+
c-axis
H2O
c-axis
Ti4+
Ti4+
H2O
twin boundary
formation
occlusion of
α-AlOOH crystals
Ti4+
H2O
Ti4+
H2O
rutile
III.
TiO2
H2O
H2O
TiO2
corundum
primary twin
equilibration
H2O
H2O
formation of
secondary twins
dehydration
of diaspore
rutile

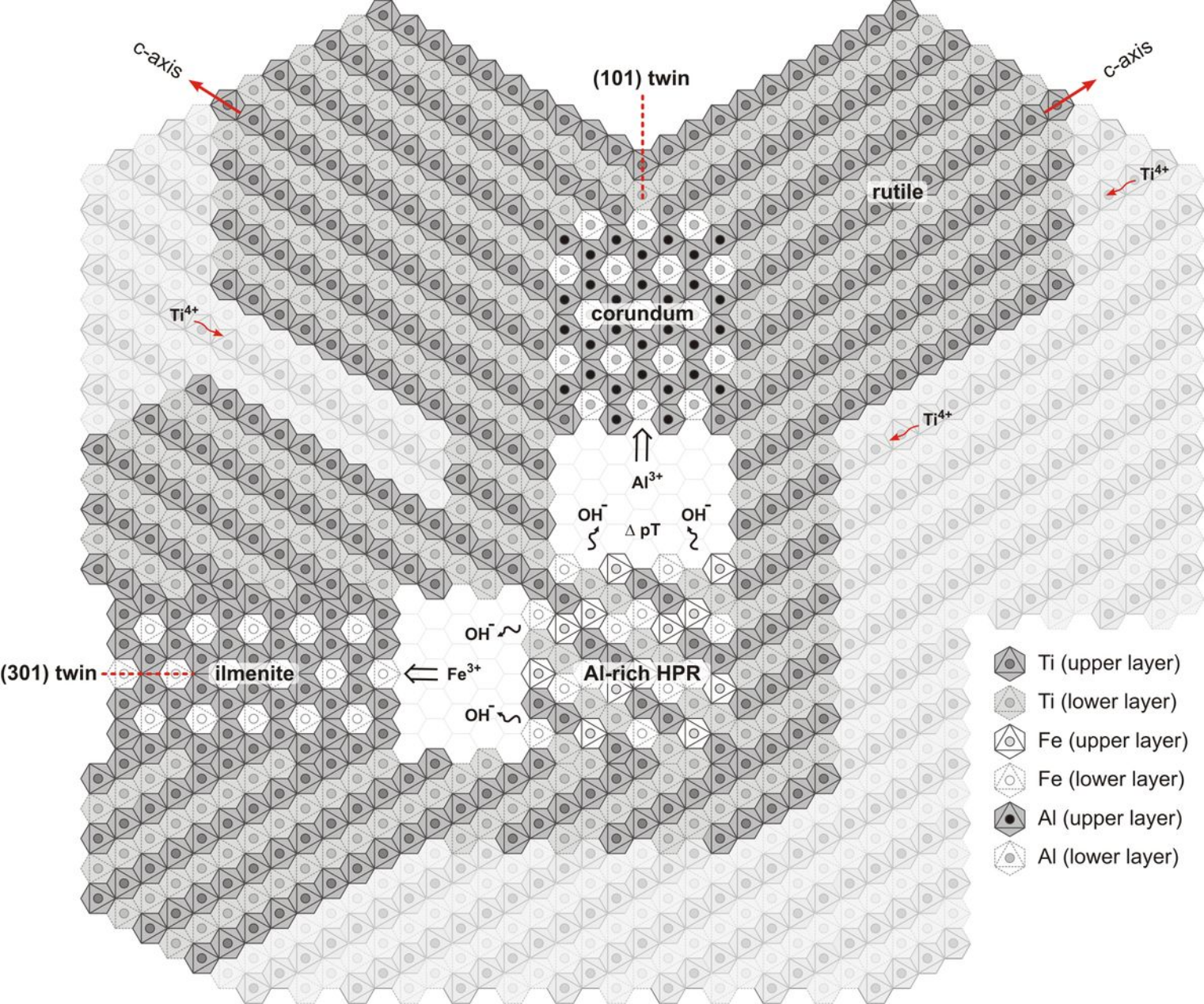
c-axis
(101) twin
c-axis
rutile
Ti4+
Ti4+
corundum
Ti4+
Al3+
OH-
Δ pT
OH-
OH-
(301) twin
ilmenite
Fe3+
Al-rich HPR
OH-
Ti (upper layer)
Ti (lower layer)
Fe (upper layer)
Fe (lower layer)
Al (upper layer)
Al (lower layer)